2/55

PROGRESS TOWARDS ESTIMATING INFILTRATION AND DEEP PERCOLATION AT THE YUCCA MOUNTAIN SITE

Prepared for

Nuclear Regulatory Commission
Contract NRC-02-93-005

Prepared by

Amvrossios C. Bagtzoglou
Stuart A. Stothoff
Michael A. Muller

Center for Nuclear Waste Regulatory Analyses
San Antonio, Texas

October 1995

ABSTRACT

This numerical modeling study was motivated by the need to obtain estimates of infiltration and deep percolation rates for the Yucca Mountain (YM) site, to understand the impact of spatial or temporal averaging, to determine the hydraulic parameters that most significantly influence the calculation of net infiltration, and to evaluate the hydrologic role of selected structural features (e.g., the Paintbrush Tuff nonwelded unit and the Solitario Canyon fault). The shallow infiltration study employed numerical simulations of coupled moisture and energy transport in homogeneous porous media and evaluated responses of the near-surface soil profile. A ten-year sequence of weather data from the Desert Rock, Nevada meteorological station was used. The simulations indicate that alluvial covers with higher values of permeability allow less liquid water to percolate in the deeper parts of the rock due to rate-limiting evaporation. A deep percolation study was also conducted that addressed the effect of spatial and temporal averaging of infiltration on the speed with which a moisture front propagates within a block of homogeneous rock. This study demonstrates that increasing spatial focusing of infiltration does not necessarily translate to increased moisture plume speeds or penetration depths since extensive lateral flows are initiated under such conditions. Finally, a numerical study of deep percolation at the YM site was conducted. Two vertical, west-east cross sections were extracted from the current version of the Center for Nuclear Waste Regulatory Analyses hydro-geostratigraphic model of YM and results from two-dimensional flow simulations, testing several focused recharge cases, were analyzed. This study provides an improved probability density function for percolation through the repository horizon at the two cross sections studied and demonstrates that focusing recharge along the Solitario Canyon fault area increases the lateral flow component but does not affect substantially the magnitude or statistical nature of the flux at the repository level.

4/55

CONTENTS

5/55

FIGURES

FIGURES (Cont'd)

7/55

ACKNOWLEDGMENTS

This report was prepared to document work performed by the Center for Nuclear Waste Regulatory Analyses (CNWRA) for the Nuclear Regulatory Commission (NRC) under Contract No. NRC-02-93-005. The activities reported here were performed on behalf of the NRC Office of Nuclear Material Safety and Safeguards (NMSS), Division of Waste Management (DWM). The report is an independent product of the CNWRA and does not necessarily reflect the views or regulatory position of the NRC. Technical reviews by Drs. R. Manteufel and G. Wittmeyer and a programmatic review by Dr. B. Sagar helped improve the quality of this document.

QUALITY OF DATA, ANALYSES, AND CODE DEVELOPMENT

DATA: No CNWRA-generated original data are contained in this report. Sources for other data should be consulted for determining the level of quality for those data.

ANALYSES AND CODES: The BREATH and BIGFLOW computer codes were used for analyses contained in this report. These computer codes are controlled under the CNWRA Software Configuration Procedures.

8/55

1 INTRODUCTION

Determining compliance with the performance objectives for both the repository system and the Geologic Setting (GS) requires prediction of groundwater flow. Since infiltration is the primary source of water in the unsaturated zone at Yucca Mountain (YM), Nevada, the amounts and locations of infiltration are controlling factors in the movement of groundwater throughout the GS. Recent total-system performance assessments of the proposed geologic repository for high-level nuclear waste (HLW) at YM, Nevada generally agree that the calculation of cumulative releases to the accessible environment over 10,000 yr is highly sensitive to the deep percolation rate, or net liquid flux through the repository [Nuclear Regulatory Commission (NRC), 1992, 1995; Sandia National Laboratories, 1992, 1994; Electric Power Research Institute (EPRI), 1990, 1992]. In all of these performance assessments, however, the magnitudes and distributions of infiltration rates used in the calculations have largely been based on assumptions and heuristic arguments. Moreover, these infiltration rates assume both spatially and temporally averaged values.

In fractured, unsaturated rock, such as that found at the YM site, occurrence of infrequent, high-intensity rainfall events may modify, perhaps drastically, the subsurface flow regime from the one predicted by assuming that all rainfall events have averaged intensities. Indeed, the Department of Energy (DOE) has concluded that the spatial and temporal distribution of infiltration may be the most important factors influencing groundwater flow path development (U.S. Department of Energy, 1992). Deep percolation fluxes are affected by processes active in the near-surface zone, including evaporation, transpiration, liquid flow, and vapor flow. Each of these processes is governed by several factors. For example, precipitation has been found to vary substantially over the YM region, both spatially and temporally, and winter storms are, in general, more uniform and of longer duration than summer storms (Hevesi et al., 1992a,b; 1994b). These observations indicate that, especially for summer storms, a spatially uniform precipitation pattern is clearly not applicable. A first step towards characterizing the spatial variability of potential recharge was presented by Flint and Flint (1994), in which the unsaturated hydraulic conductivity was estimated for the top layer in each grid block in the Wittwer et al. (1993) three-dimensional (3D) site model. Using the depth at which seasonal variations of moisture content in the porous media diminish as a reference depth, the present-day moisture contents at the reference depth were used to assess the unsaturated hydraulic conductivity. Applying a unit-gradient assumption to this hydraulic conductivity, and neglecting fracture flow, yields an areally averaged flux of 1.4 mm/yr.

Specifically, the total-system performance assessment conducted by the NRC, under the auspices of the second phase of the Iterative Performance Assessment (IPA), reached some significant conclusions directly pertinent to the infiltration issue. These, according to Manteufel and Baca (1995), are:

(i) Infiltration rate has the highest correlation with the overall system performance, that is, with calculation of the Complementary Cumulative Distribution Function (CCDF) for cumulative release

(ii) The time of liquid water contact with waste packages has a high correlation with overall system performance

(iii) Pitting and crevice corrosion potentials, as well as solubility and alteration rates, have high correlations with overall system performance

The first conclusion provided the motivation for more detailed study of infiltration processes. Recent efforts at the Center for Nuclear Waste Regulatory Analyses (CNWRA) under the third phase of IPA are concentrating on several aspects of this issue: (i) elicitation of future climate (DeWispelare et al., 1993); (ii) study of climate-linked infiltration (Gureghian et al., 1994); (iii) shallow, near-surface infiltration (this study); and (iv) deep percolation (this study). The two latter studies, namely the shallow infiltration and deep percolation, deal primarily with estimating the rate, distribution, and patterns of flow (i.e., flow velocities and their statistics) associated with the infiltration of water at the YM site. The remaining two IPA Phase 2 conclusions require a detailed understanding of where liquid water accumulates at the YM site and the amounts of liquid water available (as expressed in terms of saturation) at, or near, the proposed repository as a function of time. The saturation level at, or near, the repository is a key parameter that controls the potential for initiation of aqueous corrosion. DOE, for example, in its plans for the 1995 Total System Performance Assessment assumes the initiation saturation (i.e., the value below which no corrosion occurs) to vary between 65 and 75 percent (Wilson et al., 1994).

This numerical modeling study was motivated by the need to provide physically based estimates of infiltration rates for the YM site, to understand the impact of spatial or temporal averaging, to determine the meteorologic parameters that most significantly influence the calculation of net infiltration, and to evaluate the hydrologic role of selected structural features (e.g., the Paintbrush Tuff nonwelded unit and the Solitario Canyon fault). Furthermore, several performance-related issues are also investigated in the course of this study. These are: (i) testing the validity of the commonly made assumption that flow at the YM site is predominantly one-dimensional (1D) and vertical; (ii) estimating the distribution of fluxes in the vicinity of the repository (i.e., loguniform versus exponential flux distribution assumption); and (iii) estimating saturation time histories at the repository horizon.

Addressing all these issues clearly satisfies, to a great extent, one of the primary objectives of IPA Phase 3, which is to provide support for the evaluation of DOE's Waste Isolation Strategy (WIS) and selected DOE key uncertainties. Specifically, the work presented here addresses various aspects of the following DOE WIS components and key uncertainties: (i) Waste Package Environment—*Focusing/channeling of infiltration flux*, (ii) Radionuclide Migration in Geosphere—*Magnitude of infiltration flux* and *Travel time of water in unsaturated zone*, and (iii) Thermal Effects—*Near-field humidity*.

This report is organized as follows. First, a summary of the shallow infiltration study is presented. This section describes some counter-intuitive results, which indicate that media with higher values of permeability allow less liquid water to percolate in the deeper parts of the rock. This counter-intuitive behavior, which was explained only very recently, rendered the full coupling of the shallow infiltration and deep percolation studies impossible. There was very little justification for using results from the shallow infiltration study as boundary conditions for the deep percolation study, until this peculiar behavior was fully understood. Nevertheless, the two studies were at least to some degree coupled in the sense that the net infiltration values used in the deep percolation study were similar to, and bounded to some extent by, the results of the shallow infiltration study. Second, a pilot deep percolation study is presented that addresses the effect of spatial and temporal averaging of infiltration on the speed with which a moisture front propagates within a block of homogeneous rock. Third, two vertical, west-east cross sections have been extracted from the current version of the CNWRA hydro-geostratigraphic model of YM and results from two-dimensional (2D) flow simulations, testing several focused recharge cases, are presented.

10/55

2 SHALLOW INFILTRATION AT YUCCA MOUNTAIN

Numerical simulation of water and energy balance across the air-soil interface is one avenue being considered in order to provide boundary conditions for simulations of deeper flows. Due to the very long time frame for HLW simulations, computational efficiency in such near-surface simulators is of practical importance, as is limiting of the total number of simulations. A procedure for minimizing the number of simulations is outlined in Section 2.1, using a 1D numerical simulator to construct a response surface for infiltration as a function of hydraulic parameters, vegetation, and climatic forcings. In Sections 2.2 and 2.3, the numerical simulator and meteorological data are discussed. In Section 2.4, an example response surface for infiltration as a function of hydraulic parameters is presented, for the case of a generic semi-infinite alluvium, representative of a minimally vegetated wash with a deep alluvium cover. The behavior of the response surface exhibits a counter-intuitive dependence on permeability, in that higher-permeability media exhibits less net infiltration than lower-permeability media. In order to build confidence in the predictions of the simulator, it is important to understand any counter-intuitive behavior before approaching more complex problems; accordingly, in Section 2.5 this behavior is explained using a simplified model. Conclusions drawn from the study are summarized in Section 2.6.

2.1 FRAMEWORK FOR INVESTIGATION

The work presented here is a portion of an overall task intended to analyze meteorological and hydrological data at YM in order to estimate the spatial and temporal variation of the infiltration rate over the surface of the YM site. The intended approach for this analysis consists of using a one-dimensional numerical model incorporating physics appropriate to the near-surface environment. The 1D model is applied to a set of columns with hydraulic properties representative of the YM site. A synthetic long-term data set, based on existing short-term meteorological data, is constructed to examine the long-term response of the generic columns to meteorological and climatic forcings. Using the simulator and the meteorological inputs, a response function for long-term net infiltration below the root zone is constructed as a function of climatic conditions, hydraulic properties, and vegetative conditions. By considering distributions of the hydraulic properties over YM, distributions of long-term net infiltration are obtained directly from the response surface through interpolation, as a final processing step. This approach avoids performing a computationally demanding simulation for each possible combination of parameters.

It is anticipated that greatest infiltration will occur in regions where highly fractured tuffs outcrop or are minimally covered. However, in order to establish a procedure for examining shallow infiltration, and to identify computational efficiencies, the simplest shallow-infiltration scenario was examined first, in which fast pathways (e.g., fractures), layering, and vegetation were neglected. An actual ten-year sequence of hourly meteorological data from Desert Rock, NV, was used to provide realistic atmospheric boundary conditions. As net infiltration is expected to be highest in areas with relatively higher permeablity surface media, the most permeable porous medium at YM, alluvium, is examined. Thus, the results presented here would be most representative of washes with a deep alluvium cover and minimal vegetation. The range of permeabilities considered extends farther than expected for alluvium, into the range appropriate for an equivalent fracture continuum, in order to begin to gain some insight into the impacts of fracture flow. A more-detailed examination of the impacts of fracture flow, layering, climatic variability, and vegetation will be considered in future work.

In examining preliminary simulations, the sensitivity of infiltration to permeability was found to be counter-intuitive, in that higher-permeability media exhibited less net infiltration than

lower-permeability media. In order to build confidence in the predictions of the simulator, it is important to understand any counter-intuitive behavior before approaching more complex problems. Accordingly, in this report the counter-intuitive behavior is reproduced in a simple model, where it can be examined in detail, supplementing the sensitivity information gathered for all hydraulic parameters. The simple model suggests that lower-permeability media are less able to retrieve moisture from depth to feed evaporative demands, thereby leaving more water for infiltration.

2.2 NUMERICAL SIMULATOR

A 1D finite element model of coupled moisture and energy transport in a porous medium, BREATH (Stothoff, 1995), was used to simulate the response of the near-surface soil profile. The simulator couples the Richards equation with diffusive vapor transport, assuming local equilibrium between vapor and liquid. The energy transport model considers diffusive flux in the matrix as well as advective transport of energy via liquid and vapor fluxes. The simulator is based on model equations presented by Fayer and Jones (1990), which are further derived from an extensive soil science literature (Richards, 1931; Philip and de Vries, 1957; Gee, 1966; Sasamori, 1970; Jury, 1973; Sophocleous, 1978; Milly and Eagleson, 1980). Equation development and various test examples are presented in the user documentation of the BREATH code (Stothoff, 1995).

2.3 METEOROLOGICAL INPUT DATA

Atmospheric forcings were based on a ten-year sequence, March 1984 through February 1994, of hourly weather readings from the National Weather Service Station at Desert Rock, Nevada. The Desert Rock station is at an elevation of 1,000 m, while YM ranges in elevation from 1,250 m to nearly 1,800 m, thus the readings are presumably somewhat warmer and drier than would have been observed on YM proper. The readings include atmospheric temperature, relative humidity, wind speed, total cloud cover, and an hourly rainfall rate code. Shortwave and longwave radiation were estimated from the hourly values of cloud cover. The calculated radiation values were not compared to field measurements, but vary realistically with the other weather parameters so that the effects of time averaging are reasonable. Daily Desert Rock precipitation totals are also available; these were disaggregated into hourly values using the hourly rainfall rate code. The atmospheric variables available to the simulator on an hourly basis include precipitation, 2-m elevation atmospheric temperature (2-m above ground surface), wind speed, vapor density, and incident longwave and shortwave radiation. The atmospheric data set has an average precipitation of 160 mm/yr, average temperature of 17° C, average vapor density of 4.5×10^{-6} gm/cm^3, average incident longwave radiation of 320 W/m^2, average incident shortwave radiation of 250 W/m^2, and average wind speed of 4.1 m/s.

In arid and semi-arid regions, distinct evaporation phases can be readily identified (see Section 2.5). Immediately following rainfall events, the soil is moist enough that the atmospheric conditions determine evaporation rates. Once the top of the soil column dries out, evaporation is controlled by how fast the soil can deliver water vapor to the exposed ground surface. Extensive simulations have revealed that once the surface dries after a precipitation event, long-term average conditions are sufficient to capture the atmospheric boundary conditions, but hourly information is necessary in the periods of time immediately surrounding precipitation events. Accordingly, a strategy of imposing one-month averaging to the atmospheric conditions is followed, except in the one day immediately prior to and following each precipitation event. Simulations using this strategy run several times faster than simulations using the raw hourly data, and, depending on the porous medium, the difference in predictions of long-term average

infiltration ranges from negligible to a maximum of about ten percent. The deviation tends to become larger for situations with larger net infiltration rates.

2.4 SENSITIVITY OF INFILTRATION TO ALLUVIAL PARAMETERS

YM is characterized by a series of ridges and washes. Due to the steep wash slopes, it is anticipated that overland flow will find its way to the wash bottoms, filled with less than 20 m of potentially transmissive alluvium in most places. Therefore, it is of interest to determine what types of infiltration might be expected through the alluvium layer. The intent of the analysis is to relate long-term net infiltration and long-term average moisture content in a semi-infinite homogeneous alluvium to various hydraulic property combinations. No attempt is made to consider vegetation, layering, fast flow pathways, or deviations from the Desert Rock weather, although these factors will be quite important in characterizing actual infiltration.

The sensitivity to hydraulic parameters, including permeability (k), porosity, bubbling pressure (Po), and the van Genuchten *m* scaling parameter are investigated here. Guertal et al. (1994), Hudson et al. (1994), Hevesi and Flint (1993), and Hevesi et al. (1994a) report hydraulic properties for alluvia found in the YM vicinity. Based on these references, six permeabilities (10^{-2}, 10^{-3}, 10^{-4}, 10^{-5}, 10^{-6}, 10^{-7} cm^2), three porosities (0.2, 0.3, and 0.5), three bubbling pressures (10^4, 2×10^4, 5×10^4 Pa), and three van Genuchten *m* values (0.1, 0.2, 0.3) were considered. The permeability range extends above and below the reported values. For comparison, the permeability of clean sands ranges from 10^{-8} through 10^{-5} cm^2 and ranges from 10^{-6} to 10^{-3} for gravels (Freeze and Cherry, 1979). Consideration of media with permeabilities less than 10^{-7} cm^2 is presumed redundant based on the dramatic behavior of simulations for the 10^{-7} cm^2 media. The lower porosity is somewhat below reported values and the van Genuchten parameters are representative of the reported values. Residual moisture contents were not presented in the references; all residual moisture contents are here assumed to be zero.

In order to approximate the long-term net infiltration and long-term average moisture contents in a semi-infinite alluvium, the BREATH code is used to simulate the response of a finite-length vertical column. A 30-m column is considered, with a top element of 2 cm and element lengths smoothly increasing with depth. At the bottom of the column, a gravity-drainage, or zero-saturation-gradient, boundary condition is applied. In most cases, a 30-m column is sufficiently deep to provide a substantial extent of gravity drainage above the bottom boundary, isolating the surface dynamics from the influence of the bottom boundary and thereby adequately simulating a semi-infinite medium. A top element of 2 cm was found to be sufficiently refined to capture the surface dynamics for the range of permeabilities considered. A few combinations of material properties achieved gravity drainage quite close to the surface; these cases were run with a refined grid and shorter column to better capture surface dynamics.

Simulations were run by cycling the ten-year weather data until the average moisture flux for a decade was constant to within a few percent over the depth of the column. In the high-infiltration cases, this occurred within decades, regardless of initial conditions. In low-infiltration cases, a true cyclic steady state can take centuries to millenia of simulated time to achieve, depending on initial conditions, so periodic restarts with manually adjusted initial conditions were used to help along moisture contents in deeper zones. In the top meter or two, equilibrium conditions are achieved within the first decade or two for all cases considered. The set of long-term infiltration results are shown in Figures 2-1, 2-2, and 2-3 where the long-term net flux through the column is plotted versus the long-term average moisture content at the bottom of the column. The most striking feature of Figures 2-1, 2-2, and 2-3 is a strong trend

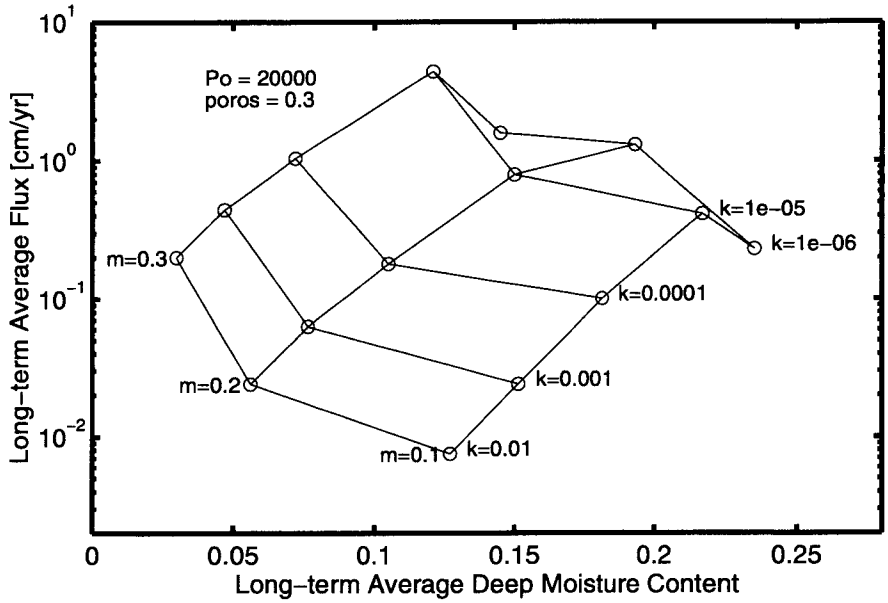

Figure 2-1. Sensitivity of long-term moisture content and moisture flux to permeability and van Genuchten *m*

towards increasing long-term infiltration and increasing average saturation with decreasing permeability for the higher values of permeability considered, when all other hydraulic parameters are held constant. The trend is apparent for each set of parameter values studied. Figures 2-1, 2-2, and 2-3 correspond to the van Genuchten *m*, porosity, and bubbling pressure of the medium, respectively. The trend is sharply broken, however, for the lowest value of permeability considered, 10^{-7} cm^2 (not plotted); such columns are almost dry, with little more moisture than required to maintain equilibrium with the atmospheric vapor density throughout the column. Thus, the long-term flux and average saturation for the k = 10^{-7} cm^2 case are less than the values for the corresponding k = 10^{-2} cm^2 case for every combination of porosity and van Genuchten parameters considered. For the cases that did not dry out, the long-term average deep saturation ranged from 10 to 78 percent, while the average deep infiltration flux ranged from 0.043 to 27 percent of average annual precipitation. Other combinations of the same parameters would presumably yield even more extreme behavior.

The region of parameter space where decreasing permeability yields increased infiltration is characterized by permeabilities such that the soil column never or rarely achieves saturation during rainfall events. For some of the parameter combinations, there is a transition permeability zone for which decreasing permeability results in a decreased infiltration but increased saturation. The transition zone begins where permeabilities are just small enough that some rainfall events start saturating the top of the soil column. At the other end, the permeabilities are so small that even though the top of the column is saturated during rainfall events, the penetration depth of the saturation front becomes negligible and all moisture entering the column is reclaimed by evaporation.

Figure 2-2 yields insight into the sensitivity of net infiltration to porosity. As porosity decreases, net infiltration increases. With decreasing porosity, the moisture from a rainfall event penetrates further, which enables a larger portion of the moisture to escape from the surface evaporation trap. Similarly, Figure 2-3 indicates that decreasing the bubbling pressure yields higher infiltration. Interestingly,

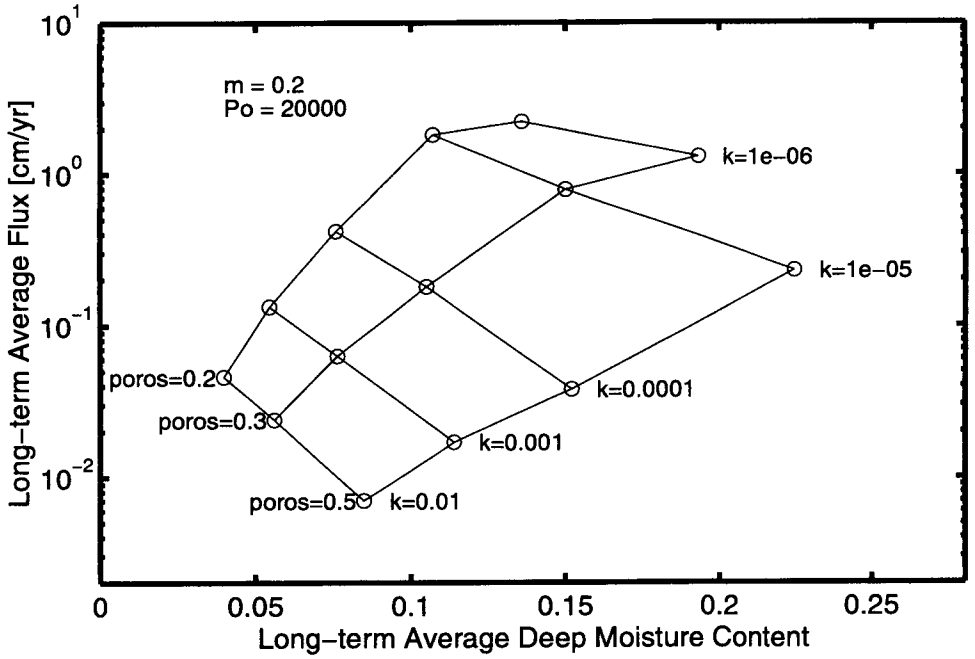

Figure 2-2. Sensitivity of long-term moisture content and moisture flux to permeability and porosity

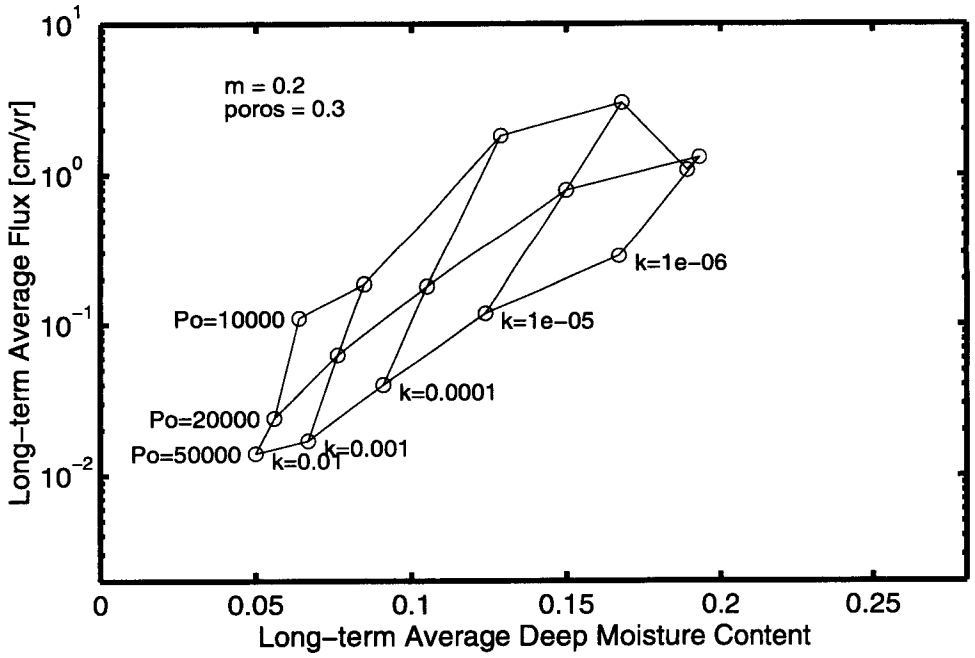

Figure 2-3. Sensitivity of long-term moisture content and moisture flux to permeability and bubbling pressure

decreasing the van Genuchten *m* parameter yields less infiltration but wetter soils. Increasing *m* and decreasing the bubbling pressure corresponds to making the medium more uniform in composition and coarser. The bubbling pressure only affects the moisture retention capacity of the soil, while the *m* parameter affects both the moisture retention and the relative permeability of the soil and accordingly has the more complex impact.

2.5 SENSITIVITY OF INFILTRATION TO PERMEABILITY

The result that infiltration decreases as permeability increases is quite surprising, as presumably wetting pulses would penetrate deeper in a more permeable material and thus be less susceptible to evaporation. The result is not unprecedented, as increasing evaporation has been linked to increasing permeablity in the presence of a water table (Czarnecki, 1990); however, in Czarnecki's work the water table provides a source of moisture at depth which is not present in the current simulations. Young and Nobel (1986) also found that increasing permeability increases evaporation; however, no explanation is offered and the lower boundary condition is not presented.

In order to study the sensitivity of infiltration to permeability, two cases shown in Figures 2-1, 2-2, and 2-3 are examined in greater detail. The cases differ only in permeability, with permeabilities of 10^{-3} and 10^{-5} cm^2, respectively. The other parameter values are in the middle of their range, so that the van Genuchten *m* value is 0.2 and the bubbling pressure is 2×10^4 Pa. As before, the simulations use cycled meteorological boundary conditions until cyclic steady state was approximated; however, for simplicity the average meteorologic conditions are used all year and all rainfall is condensed into one rainfall pulse applied at a constant rate for one day. The resultant rainfall rate is slightly less than the saturated hydraulic conductivity for the less-permeable material. A much more refined grid is used in this case, as fairly extreme infiltration conditions are applied, so that the top element is 2 mm rather than 2 cm in size. A column of 100 m is used so that there is no possible contamination of the results due to the bottom boundary.

Snapshots of the moisture content profile for the two cases are shown in Figure 2-4. The snapshots are at 0.3 d, 1 d, 0.03 yr, 0.1 yr, 0.3 yr, and 1 yr. The profiles with higher values of moisture correspond to the low-permeability medium. Two observations can be drawn from Figure 2-4. First, the high-permeability medium allows a slightly faster penetration of the wetting front during rainfall. The low-permeability medium requires a greater change in moisture content to satisfy the change in conductivity necessary to transmit the boundary flux, so more moisture goes into storage and the front is retarded. Second, the low-permeability medium achieves a drying front sooner than the high-permeability medium, and the drying front for the low-permeability medium is always deeper than the drying front for the high-permeability medium. Until a drying zone appears, both media are able to allow evaporation at near the potential-evaporation rate, but this period is shorter for the low-permeability medium. Once a drying zone appears, evaporation is rate-limited by vapor diffusion across the zone, and the evaporation rate decreases as the front advances. Accordingly, once the drying zone appears in both media, the low-permeability medium consistently evaporates at a slower rate than the high-permeability medium. Both of these factors leave more water available for net infiltration for the low-permeability medium.

2.6 CONCLUSIONS FROM THE SHALLOW INFILTRATION STUDY

Findings of this study include:

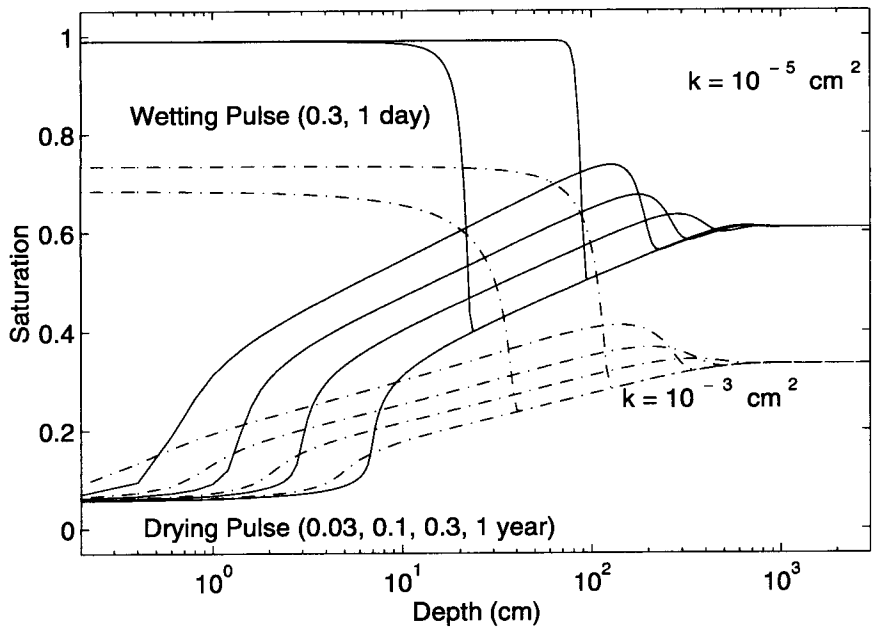

Figure 2-4. Snapshots of moisture content profile at various times for two media with permeabilities of 10^{-3} and 10^{-5} cm^2

(i) A deep alluvium (20-30 m) with permeability less than 10^{-6} cm^2 is expected to dry out, even in the absense of vegetation, thus having negligible infiltration under YM conditions.

(ii) For deep alluvia with permeabilities greater than the dryout permeability, a range of permeability spanning 5 orders of magnitude is found to have a concommitant range in net deep infiltration of nearly 3 orders of magnitude.

(iii) The 1D simulations show that net deep infiltration varies inversely with permeability for the higher-permeability media, so that permeability may be a misleading indicator of infiltration into a porous continuum.

(iv) Lower-permeability media develop an evaporation-limiting dryout zone sooner than higher-permeability media, thereby allowing less evaporation and leaving more water for net infiltration.

(v) The highest net long-term infiltration rates occur for media that saturate for only the largest rainfall events. When a medium saturates for small events, much of the rainfall is diverted into runoff and prevented from entering the soil column. When a medium easily accepts all rainfall, it also easily returns the moisture to the surface to be reclaimed as evaporation, leaving less for infiltration.

The general applicability of these conclusions is limited by the assumptions inherent in this work. These are: (i) homogeneous alluvium of sufficient thickness, (ii) 1D flow with no opportunity for lateral water movement, and (iii) vegetation and runon-runoff effects being neglected.

3 DEEP PERCOLATION IN HOMOGENEOUS ROCK

Most numerical modeling efforts related to the YM project assume that the net infiltration is uniformly distributed in space and time. The mean values used in these type of simulations do not take into account the more extreme rainfall rates that may occur due to either interannual or interseasonal fluctuations, or even individual storm events. It is hypothesized that focusing of infiltration may have a significant effect on various measures related to performance (U.S. Department of Energy, 1988).

This work examines the effects of focusing infiltration in space and time, so that the net infiltration rate remains at 100 mm/yr, bounding at the high end the range of 0.1 to 40 mm/yr predicted by the shallow infiltration study described in Section 2. This ensures that the total mass of water entering the system is preserved, but allows the infiltration rates to locally become several orders of magnitude higher. This effort will attempt to provide answers to the following questions: (i) how does moisture propagate under conditions of focused recharge in a uniform porous medium, (ii) does the temporal averaging of infiltration affect flow patterns, and (iii) what is the effect of spatial focusing and temporal amplification on travel time-related measures?

3.1 NUMERICAL SIMULATOR

The BIGFLOW (Ababou and Bagtzoglou, 1993) simulation code was used in these analyses. BIGFLOW accommodates 3D transient or steady flow in saturated, or partially saturated porous media with heterogeneous or spatially random hydrodynamic coefficients. For partially saturated flow, a mixed variable formulation of Richards' equation is used. That is

$$\frac{\partial \theta(h,\boldsymbol{x})}{\partial t} = \nabla \left[K(h,\boldsymbol{x}) \left(\nabla h + \boldsymbol{g} \right) \right] \qquad \textbf{(3-1)}$$

where h is pressure head (m), θ is volumetric water content (m^3/m^3), K is hydraulic conductivity (m/s), and $\boldsymbol{g}$ is the body force unit vector aligned with, and opposed to, the acceleration of gravity. The differential equations are discretized by an implicit finite difference scheme, two-point backward Euler in time, and seven-point centered in space. The spatial mesh is a regular rectangular lattice. The time step is generally variable and self-adjusted. The computational domain is a three-dimensional parallelepiped, whose coordinate system may be inclined at arbitrary angles with respect to the natural, horizontal-vertical coordinate system.

3.2 IMPOSING SPATIAL AND TEMPORAL FOCUSING

A homogeneous block of rock with dimensions 10x20x25 m is considered with hydraulic properties characteristic of the Calico Hills nonwelded unit. A flow problem was studied for a base net infiltration rate of 100 mm/year applied for a period of 10 yr, and two and four levels of spatial and temporal averaging, respectively. The simulation period of 10 yr was chosen in order to correspond to the ten-year weather sequence data used in the shallow infiltration study. Hydrostatic pressure head initial conditions were imposed for all the simulations reported in this section. A water table and no-flow boundary conditions were prescribed at the bottom and lateral sides of the computational domain, respectively. The different levels of averaging are classified with the help of two indices: (i) a Spatial Focusing Index (SFI), and (ii) a Temporal Amplification Index (TAI). The definition of these indices is depicted in schematic form in Figures 3-1 and 3-2 for the SFI and TAI, respectively. As indicated in

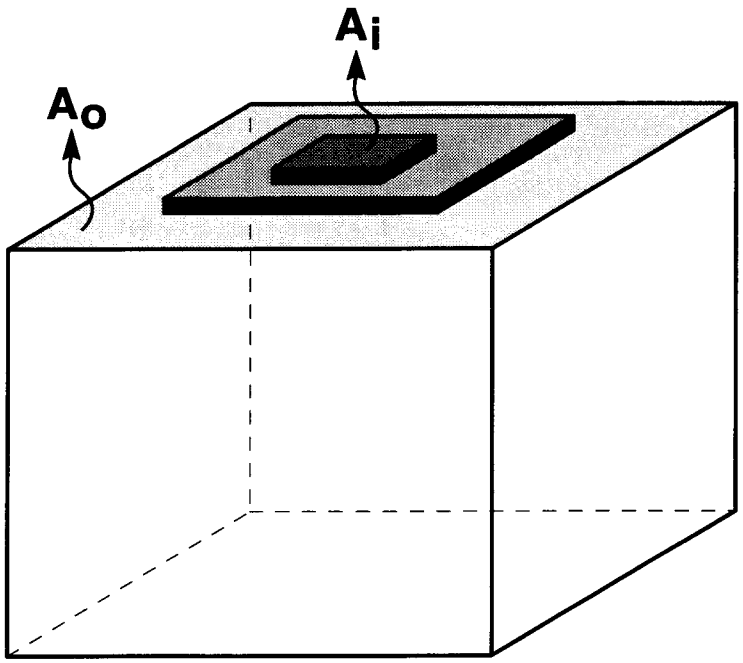

Figure 3-1. Schematic definition of the spatial focusing index (SFI)

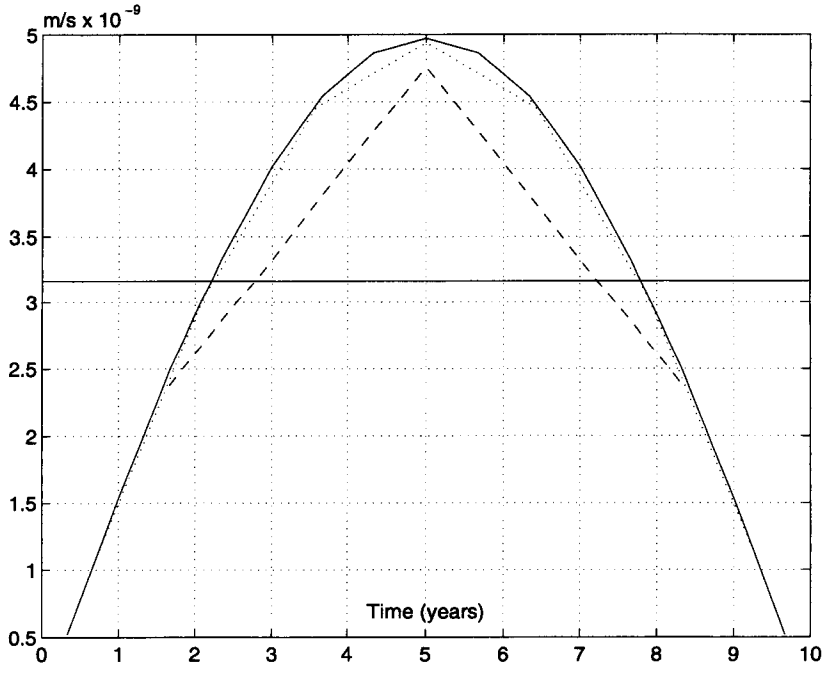

Figure 3-2. Schematic definition of the temporal amplification index (TAI) and levels used in this study. Solid (horizontal): TAI=1.00, dashed: TAI=1.50, dotted: TAI=1.56, and solid: TAI=1.57

Figure 3-1, the simulations presented herein start from a fully uniform net infiltration rate applied at an area A_0 (the total top boundary surface) at the top of the whole domain. At successive simulations, the same amount of water per unit time is applied to a smaller and smaller surface area yielding a SFI=A_0/A_i that is always greater or equal to one. More specifically, the two SFIs studied here were 4 and 17.1.

Figure 3-2 depicts the four levels of temporal averaging investigated, corresponding to an even division of the total simulation time of 10 yr in 1, 3, 7, and 15 equal intervals. Specifically, the four TAIs (defined as the ratio of maximum to mean infiltration flux for an approximately sinusoidal variation with a period of 10 yr) investigated here were 1.00, 1.50, 1.56, and 1.57.

3.3 RESULTS

Selected effects of these factors can be seen in Figures 3-3 and 3-4 and Figures 3-5 and 3-6 for a SFI of 4 and 17.1, respectively. Figures 3-3 and 3-5 depict pressure head results at the end of 10 yr of infiltration at a vertical cross section passing through the centroid of the computational domain for TAIs of 1 and 1.57. Figures 3-4 and 3-6 are somewhat similar to Figures 3-3 and 3-5 but correspond to pressure head profiles at a vertical transect passing through the centroid of the computational domain for all the TAIs investigated here. It can be seen from Figures 3-3, 3-5 and 3-4, 3-6 that increasing spatial focusing creates the effect of a moisture mound building up underneath the area where infiltration is applied. However, as the infiltration signal deviates from a constant and approaches a sinusoidal perturbation with the same volume of water, the effects of spatial focusing become less important. In order to capture the essence of these results in a very compact form the following analysis was conducted. This analysis also provided insights into the effects that the spatial and temporal averaging have on calculations of particle travel time.

A certain pressure head level was tracked in space and time for each infiltration simulation; the −15 m pressure head was chosen here. At the end of each simulation (i.e., 10 yr) the depth to which the −15 m contour level had traveled was recorded. As Figure 3-7 indicates, in schematic form, more pronounced spatial focusing leads to excessive lateral flow at the top of the domain during the beginning of the infiltration. This, in turn, results in the moisture plume traveling slower for the more pronounced spatial focusing case. Figure 3-8 presents these results in terms of depth of travel as a function of the level of temporal amplification and spatial focusing. It should be kept in mind that these results are highly dependent on the nature of the characteristic curves used and the initial conditions assumed. It is possible that under a different combination of imposed infiltration flux and initial conditions, an entirely different flow behavior may exist.

3.4 CONCLUSIONS OF THE STUDY OF DEEP PERCOLATION IN HOMOGENEOUS ROCK

Findings of this study are:

(i) The area under the focused percolation (vertical transect right underneath the centroid of the area of focusing) is substantially wetter for the higher focusing index. Furthermore, it is associated with extensive lateral flow.

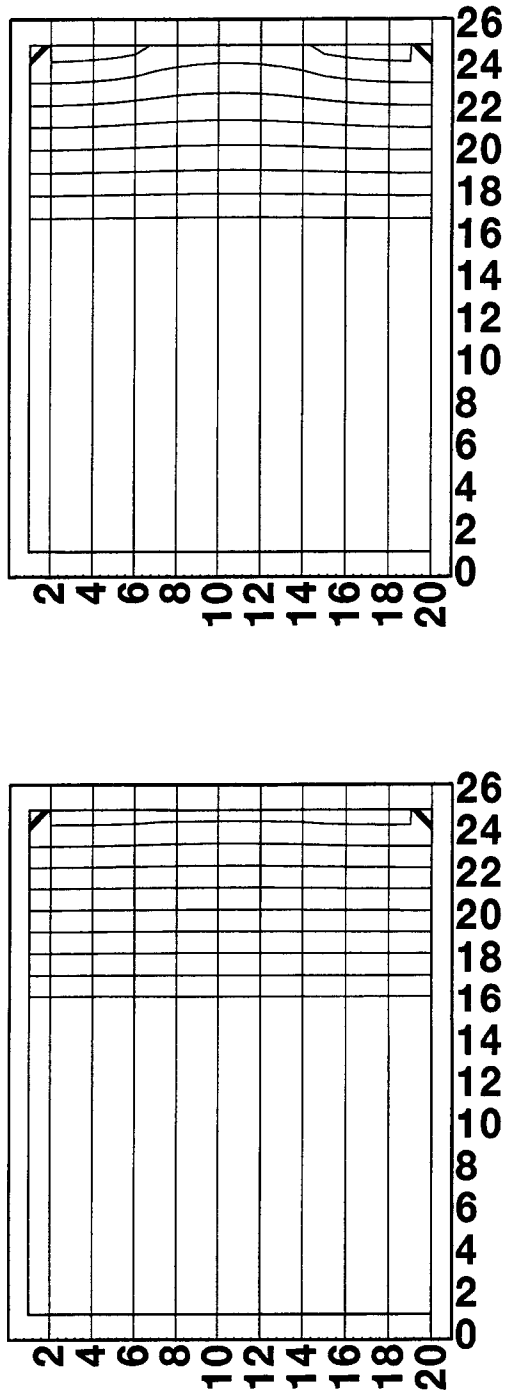

Figure 3-3. Pressure head contour after 10 yr of infiltration with SFI=4.0 and TAI=1.00 (top) and TAI=1.57 (bottom)

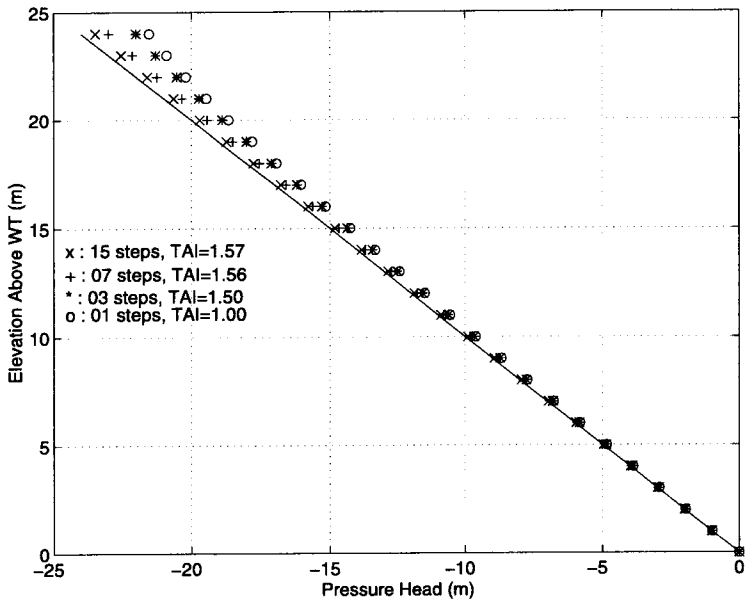

Figure 3-4. Pressure head profile at the center of the domain after 10 yr of infiltration with SFI=4.0 and various TAIs

(ii) The moisture penetration depth is consistently underestimated in cases when a temporally averaged infiltration signal is employed.

(iii) As infiltration deviates from a temporally averaged signal and approaches a sinusoidal the effects of spatial focusing on moisture penetration depth become insignificant.

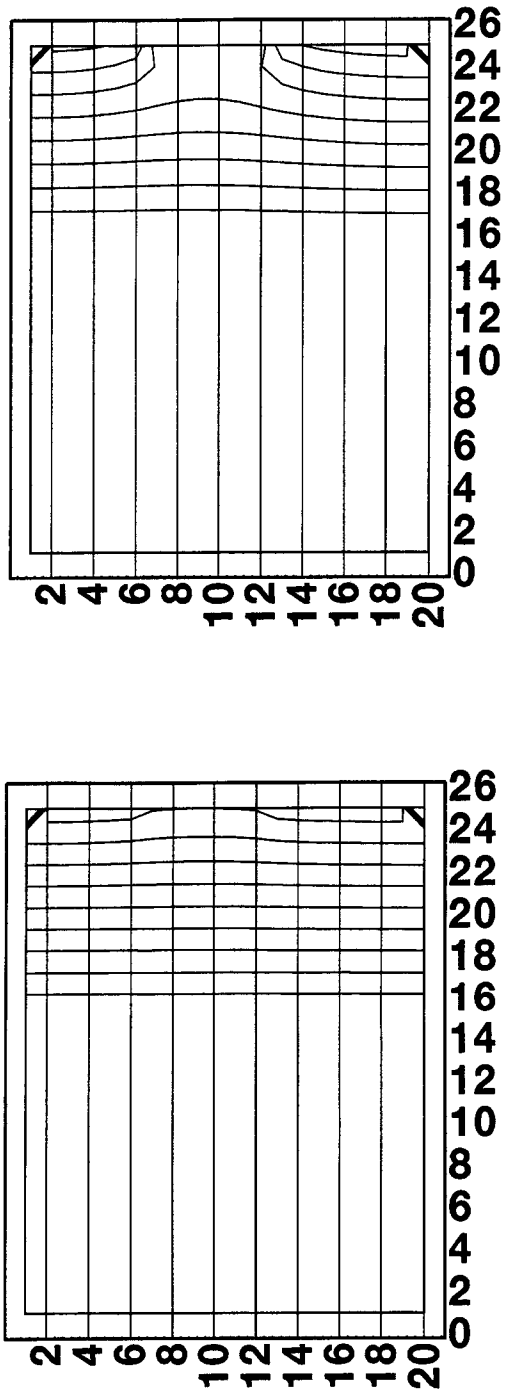

Figure 3-5. Pressure head contour after 10 yrs of infiltration with SFI=17.1 and TAI=1.00 (top) and TAI=1.57 (bottom)

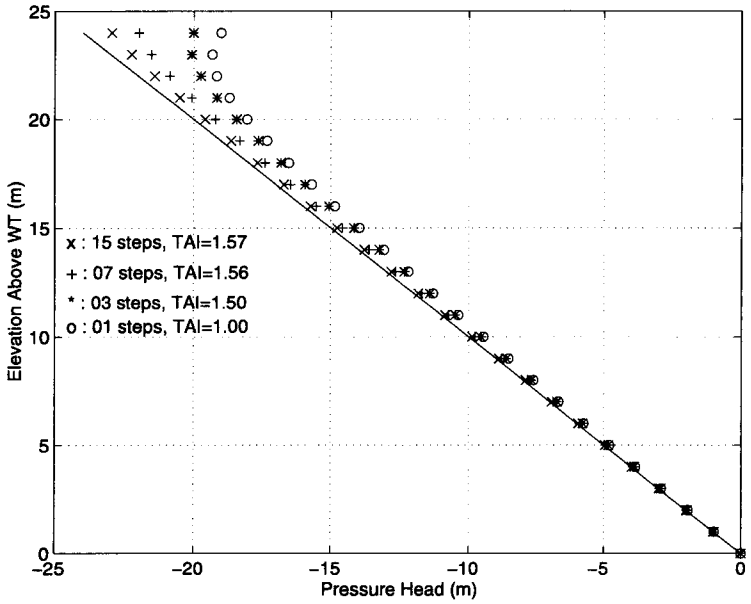

Figure 3-6. Pressure head profile at the center of the domain after 10 yr of infiltration with SFI=17.1 and various TAIs

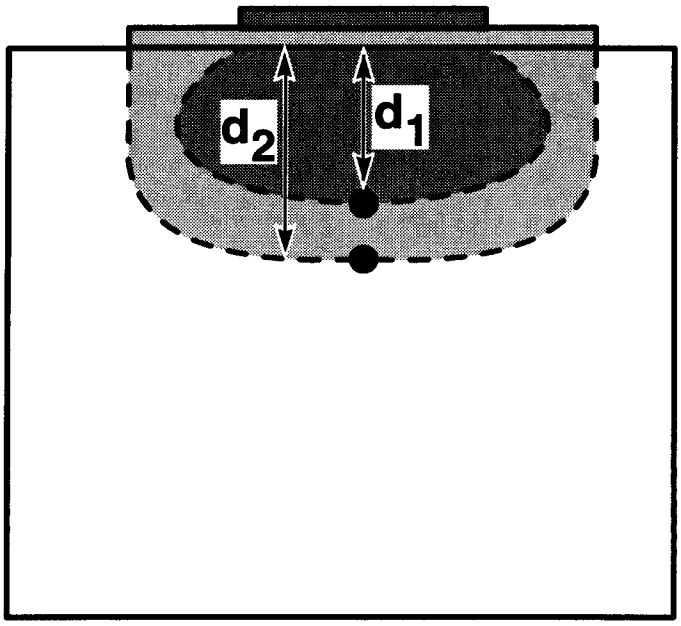

Figure 3-7. Schematic showing the calculation of the penetration depth for a specified pressure head contour level, after 10 yr of infiltration

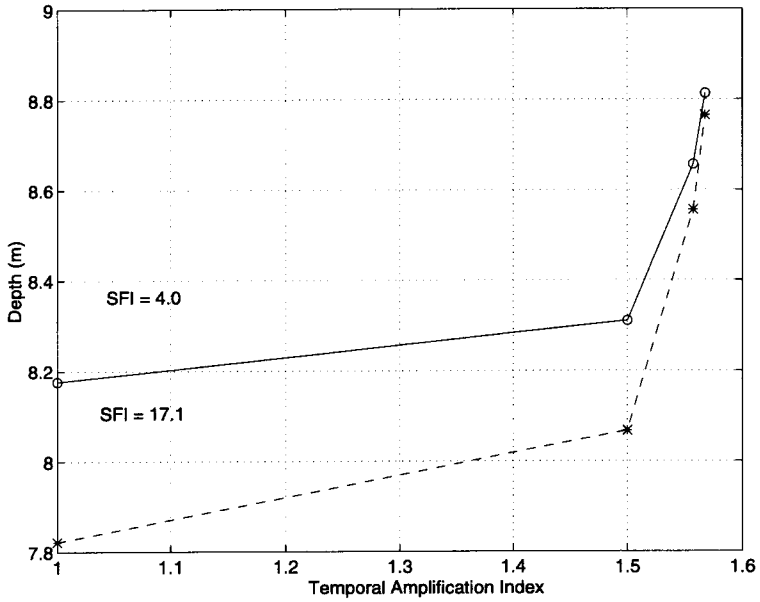

Figure 3-8. Spatial focusing and temporal amplification effects on a travel time-related measure

4 DEEP PERCOLATION AT YUCCA MOUNTAIN

This part of the study attempts to answer the following questions: (i) what is the effect of focused recharge along the Solitario Canyon (SC) fault; (ii) does the juxtaposition of dipping strata along subvertical faults provide conditions where perching or high saturations may occur; (iii) what is the saturation time history pattern at, or near, the repository; (iv) what is the hydrologic role of the Paintbrush Tuff non-welded unit; (v) is the water flux crossing the repository horizon predominantly vertical; (vi) do vertical flow patterns correspond to fast pathways; and (vii) can an improved, in terms of values and shape (e.g., loguniform versus exponential assumption of flux distribution), probability density function (PDF) for the percolation flux through the repository be obtained? These questions were addressed as follows.

4.1 GEOLOGICAL FRAMEWORK

The current version of the EarthVision 3D geological framework model described in the work of Stirewalt and Henderson (1995a,b) is used for this analysis. This model, developed using the EarthVision software, comprises a stack of the following eight lithostratigraphic units: Tiva Canyon welded (TCw), Paintbrush Tuff non-welded (PTn), Topopah Spring welded (TSw1, TSw23), Calico Hills non-welded (CHn), Prow Pass welded (PPw), Crater Flat Undifferentiated non-welded (CFUn), and Bullfrog welded (BFw). This lithostratigraphic classification follows the nomenclature of Ortiz et al. (1985). The model includes the Bow Ridge, Ghost Dance, and Solitario Canyon faults. It is based on three balanced cross sections, produced using data obtained from Scott and Bonk (1984), and eight boreholes. Figure 4-1 depicts a perspective view of the 3D model looking from South towards North. The various shades at the surface correspond to variations in the topographic relief as determined from U.S. Geological Survey digital elevation data in Digital Elevation Model format at a 30 m pixel resolution. The three subvertical faults are depicted in red and parts of the repository outline and Experimental Studies Facility (ESF) are shown in brown and blue, respectively.

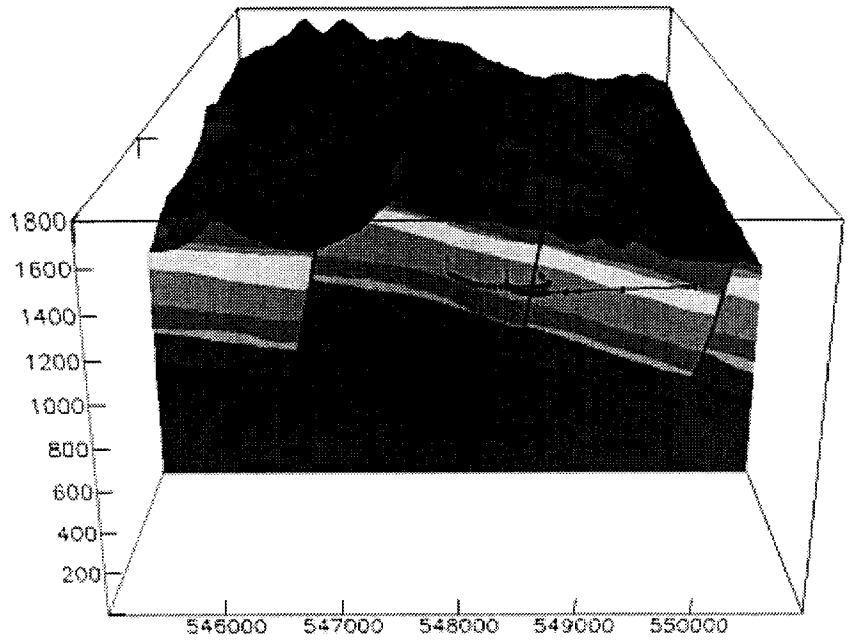

Figure 4-1. 3D geological framework model of the YM site

In order to investigate the role of important structural features, such as faults, on the hydrologic behavior of the YM site, two vertical, west-east cross sections have been extracted from the current CNWRA hydro-geostratigraphic model. The cross sections have been selected in a manner that intersect the SC fault's longitudinal axis at right angles. Moreover, they were chosen such that one intersects the repository outline at the north tip and one at the south tip, as shown in Figures 4-2 and 4-3, respectively. Cross sections A-A' and B-B' are depicted in Figures 4-4 and 4-5. The cross sections corresponding to Figures 4-2 and 4-3 were modified from the original geological EarthVision cross sections in that they were converted into digital form and discretized into a mesh of 66x29 cells so that they can form the data bases required for numerical flow simulation. The computational cell had a size of 60 and 30 m in the horizontal and vertical directions, respectively. Due to the paucity of data for the CFUn unit, the BFw and the CFUn units were combined in one with hydrologic properties equivalent to those of the BFw unit. It is worth noting that these cross sections have two important differences: (i) the offset of the geologic units along the SC fault as manifested by the normal slip along the fault is more pronounced in the south cross section (B-B'); and (ii) in the case of the south cross section (B-B') the host rock unit (TSw1, TSw23) is exposed at the east flank of SC. The final form of the two cross sections after all operations were performed can be seen in Figures 4-4 and 4-5. It should be noted that the north cross section appears to maintain geologic unit continuity across faults. This is due to the fact that the vertical resolution of 30 m cannot capture the minimal fault offsets present at this location. This difference, however, provided an extremely useful numerical avenue for evaluating the hydrologic role of faults by comparing the flow results between the two cross sections.

Representative hydraulic property values were assigned to each of the seven strata comprising the model. Only matrix properties were used and these were derived from data obtained by DOE at boreholes GU3-3, GU3-7, G4-4, G4-7, GU3-14, GU3-18, and G4-21. The SC and Ghost Dance (GD) faults were modeled only as geometric discontinuities. 2D flow simulations were conducted using the BIGFLOW numerical code, described briefly in Section 3.1, under the following three cases: (i) a relatively "wet" initial system which drains under gravity, which also served as the initial condition for the subsequent simulation cases; (ii) a uniform infiltration rate being imposed as top boundary condition over the whole mountain; and (iii) a spatially focused infiltration rate imposed over the SC fault area corresponding to a range of SFIs between 2.9 and 5.1, similar to the low end of the range studied during the pilot analysis. In all simulations the lateral boundaries are assumed to be no flow and a water table condition is prescribed at the bottom.

For all simulations, presented here, the infiltration rate varied from 0.02 mm/yr to 2 mm/yr. This range was chosen so that the results of the shallow infiltration study were captured in an average sense. Specifically, Figures 2-1, 2-2, and 2-3 depict a wide range of calculated net infiltration fluxes corresponding to variations of several material properties. The mean value of infiltration flux estimated from these figures is approximately 2 mm/yr. It is assumed that the top of the mountain has no alluvium cover at all, since the effects of alluvium cover and near-surface processes have been taken into account under shallow infiltration studies.

Finally, a variety of plots are used to present the results obtained. These plots include:

(i) Color contours of saturation, pressure head, and flow velocity magnitude. In this last type of plot the direction of flow is also depicted.

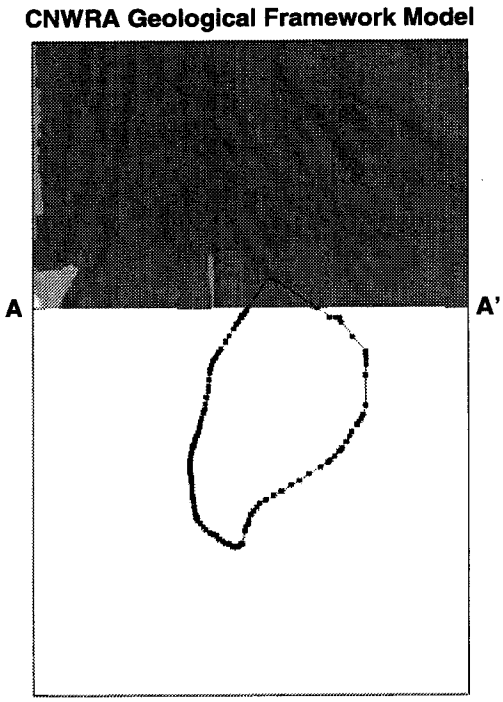

Figure 4-2. Plan view of the YM site showing the outcropping geologic units and the transect of cross section A-A'

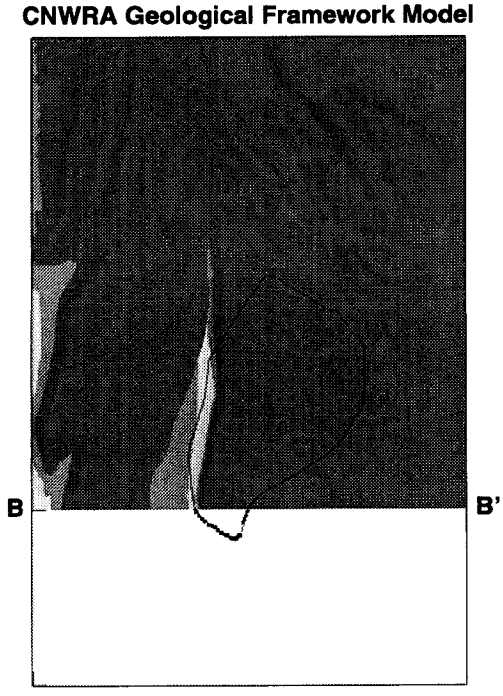

Figure 4-3. Plan view of the YM site showing the outcropping geologic units and the transect of cross section B-B'

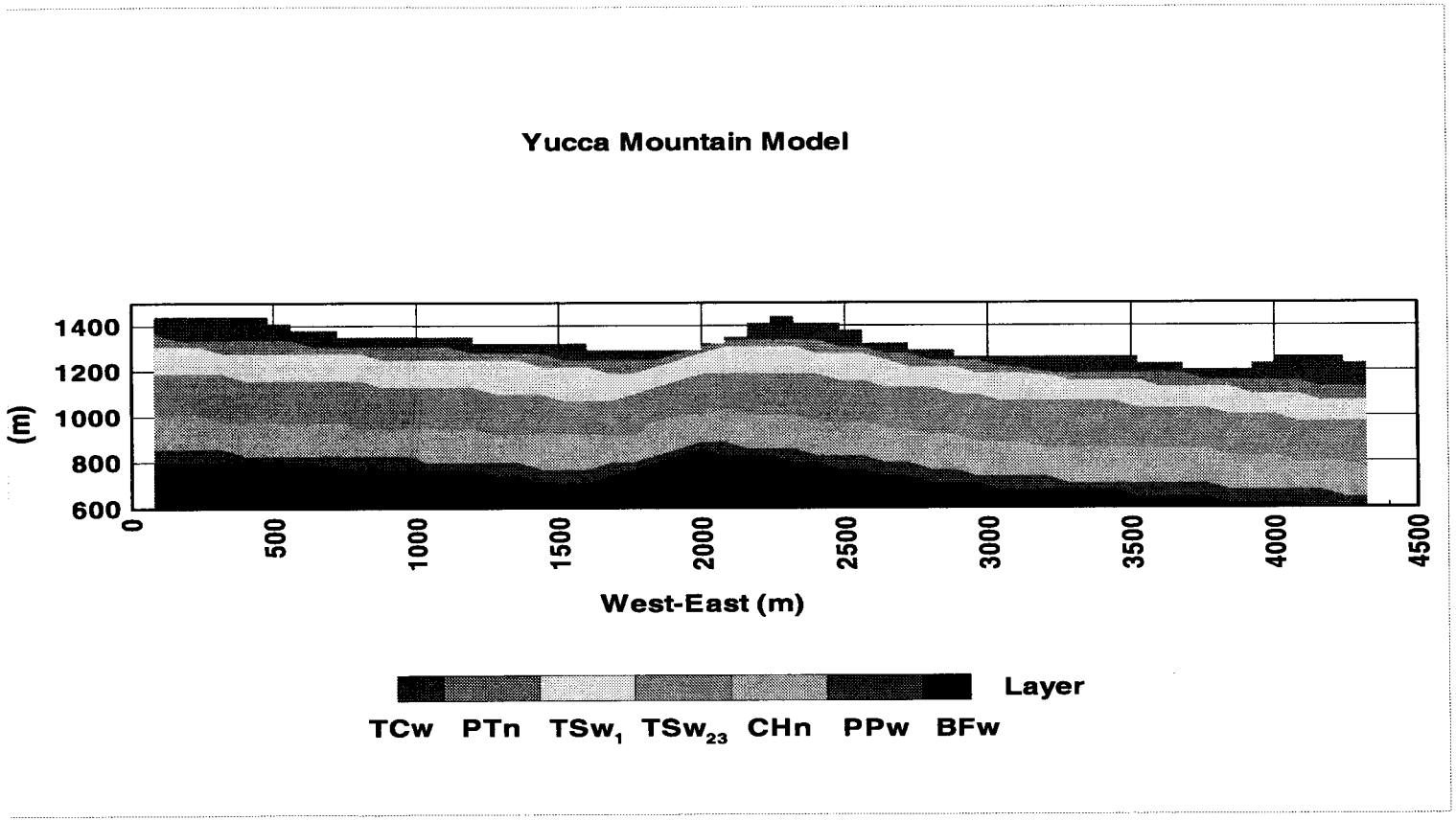

Figure 4-4. Vertical cross section A-A' as modified for the required computational resolution

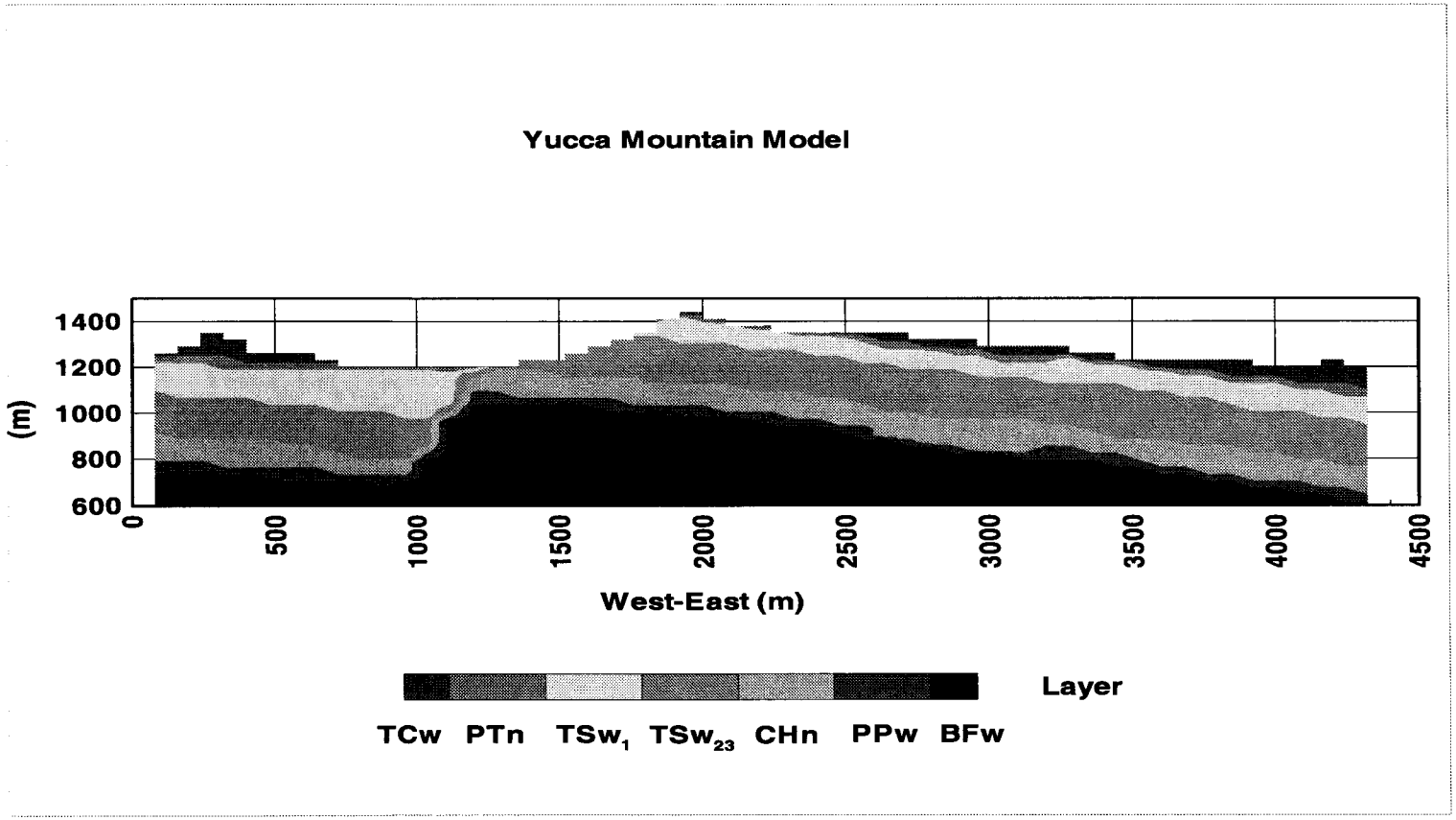

Figure 4-5. Vertical cross section B-B' as modified for the required computational resolution

(ii) Saturation as a function of time at five specific points in the vicinity of the repository. These points are the left and right tip of the repository outline at the cross section of interest, the centroid of the repository at the cross section of interest, one point one cell above the centroid of the repository, and one point one cell below the centroid of the repository.

(iii) Histograms of velocity magnitude and direction for the cross section of interest. From the information contained in the histograms one can derive a plot that resembles a phase diagram, relating the statistics of flow direction to the statistics of flow magnitude for the area under investigation. This type of plot is very useful since one can readily observe where the majority of water is flowing to and how fast it is traveling.

(iv) Also derived from histogram information, cumulative distribution functions (CDFs) can be plotted, which in the case of the flow velocity magnitude can be used to investigate the validity of the loguniform versus exponential assumption of flux distribution. Figures 4-6 and 4-7 depict, in schematic form, the relationship that exists theoretically between the nature of the PDF of the parameter in question, in real and logarithm-transformed space, and the CDF corresponding to the PDF. Depending on the shape of the CDF of the logarithm of flow velocity through the repository, one can possibly infer whether the loguniform or the exponential assumption is more realistic.

(v) Finally, comparisons between the histogram-related plots pertaining to the whole cross section and the part of the domain underneath the repository outline are useful in that they provide information on whether the flux crossing the repository is of different statistical nature than the rest of the domain. Figures 4-8 and 4-9 depict cross sections A-A' and B-B' with the repository outline intersected and identified in black color. The area that is enclosed within an imaginary rectangle bounded by the repository outline at the top, the water table at the bottom, and two vertical lines passing from the west and east tips of the repository outline is compared to the whole cross section in terms of flow patterns and associated statistics.

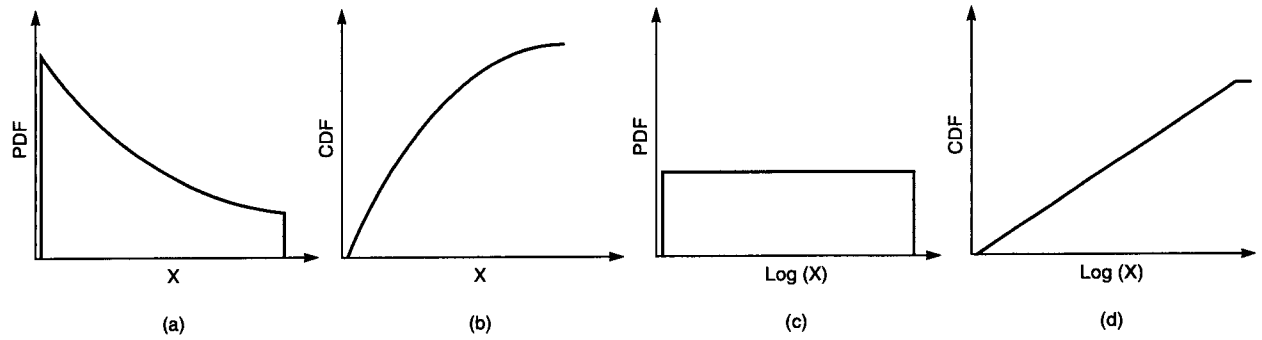

Figure 4-6. Schematic of the relationship existing between the PDF and the CDF of a loguniform distribution. a) and b) PDF and CDF of non-transformed parameter, c) and d) PDF and CDF of log-transformed parameter

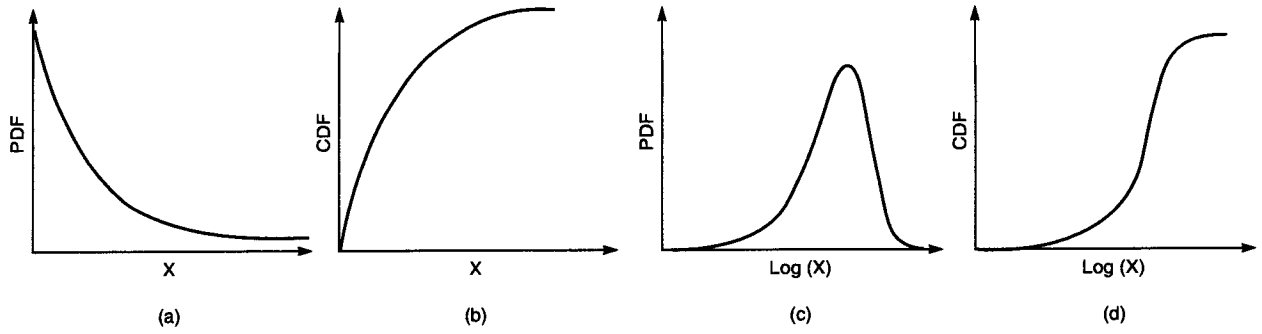

Figure 4-7. Schematic of the relationship existing between the PDF and the CDF of an exponential distribution. a) and b) PDF and CDF of non-transformed parameter, c) and d) PDF and CDF of log-transformed parameter

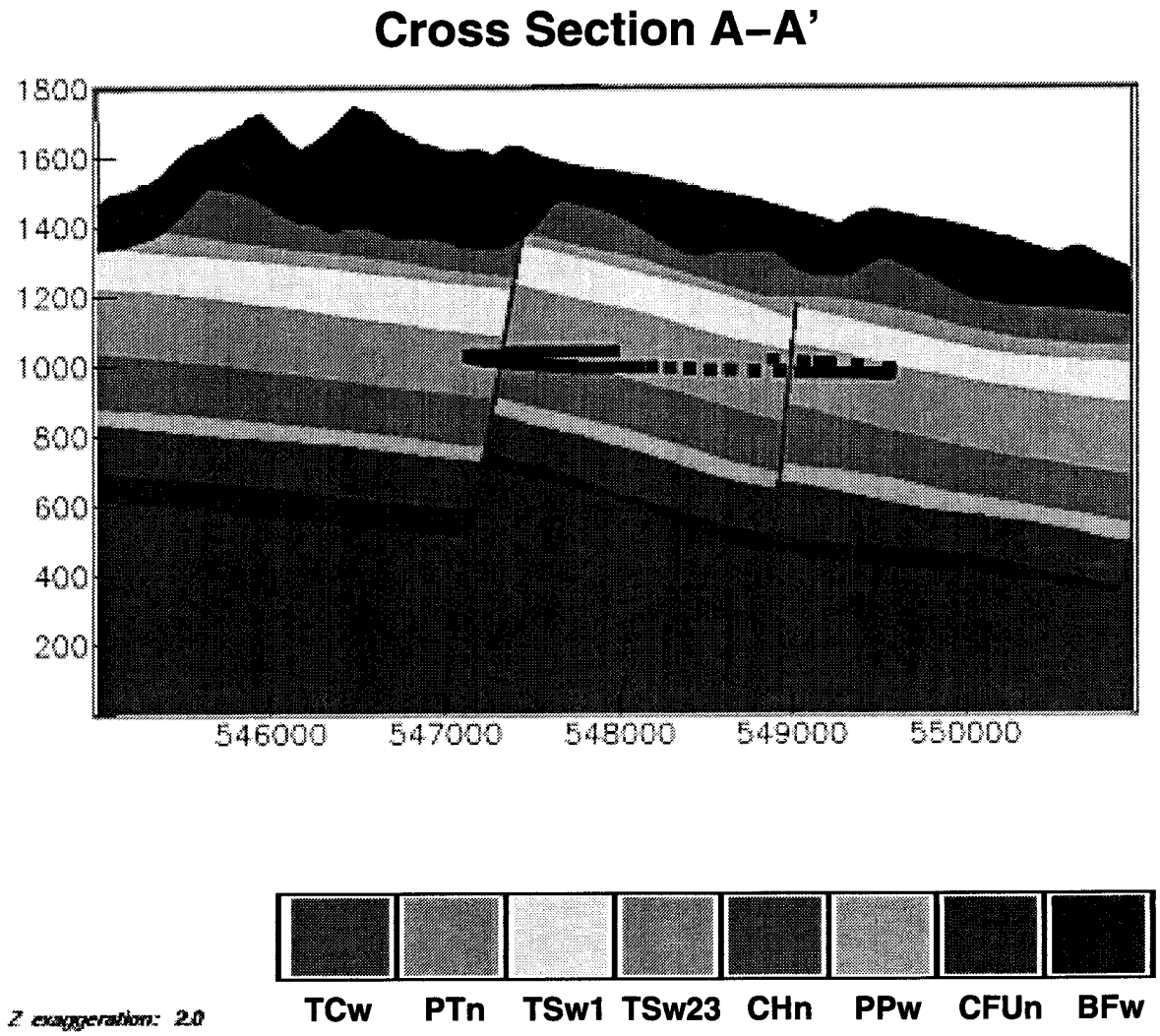

Figure 4-8. Vertical cross section A-A' running West-East with intersected repository outline identified

Cross Section B–B'

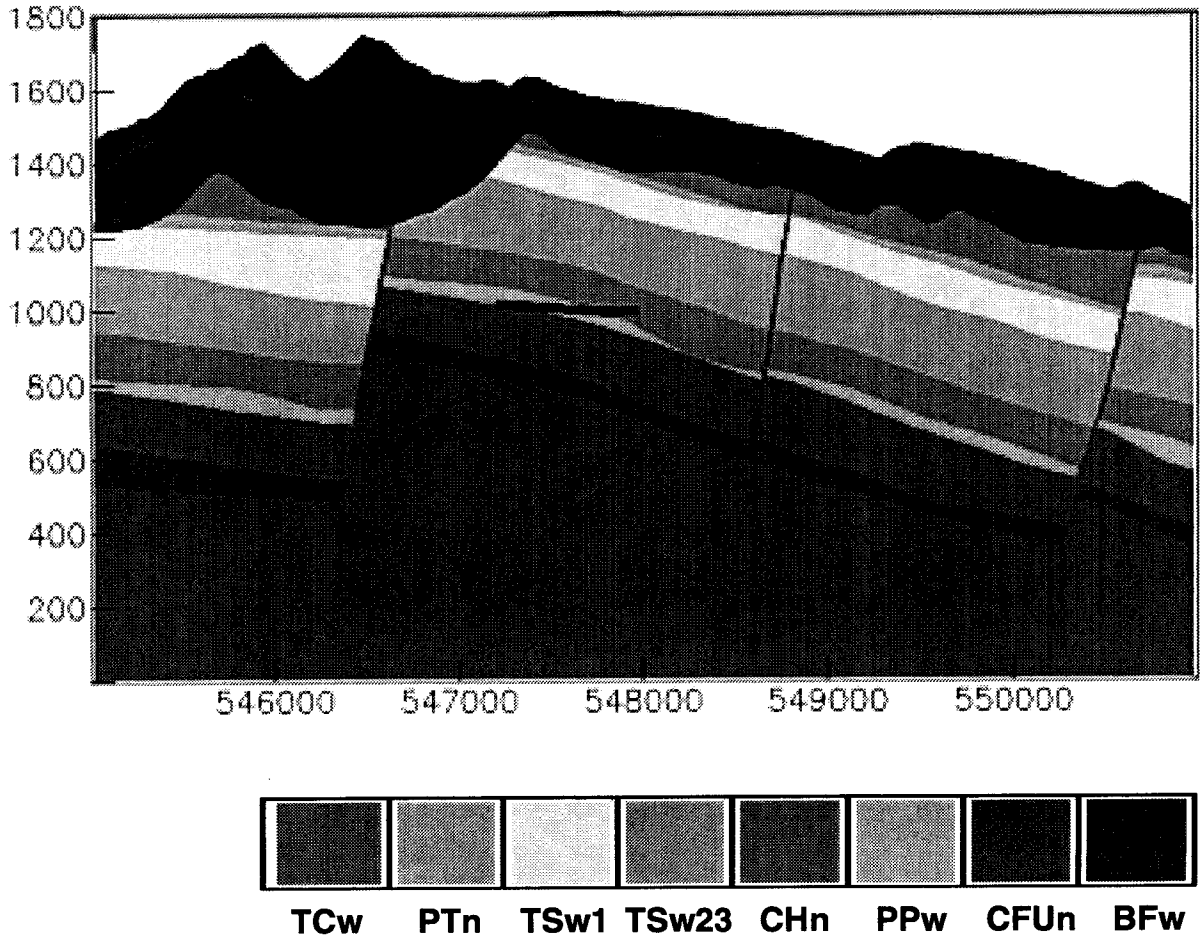

Figure 4-9. Vertical cross section B-B' running West-East with intersected repository outline identified

4.2 RESULTS

4.2.1 Non-Faulted Cross Section (A-A')

Figure 4-10 shows the results of a flow simulation for cross section A-A' at almost steady state conditions, under a uniform net infiltration rate of 0.2 mm/yr applied over the whole mountain. The initial condition for this simulation was the result of a very long draining process that served as pre-conditioning for the simulation. An almost hydrostatic distribution of pressure head is evident near the west and east boundaries of the domain. However, local perturbations from this pattern persist near the CHn-TSw interface west of Yucca Crest (the highest elevation area in the middle of both cross sections), where pressure heads near zero develop, and within the CHn unit, which is typically much drier than the adjacent units. This is an indication that this simulation has not reached an absolute steady state yet. This is corroborated by the saturation time history at the five sample points of the intersected repository outline. As can be seen in Figure 4-11, saturation at the repository horizon is increasing in three out of five points even after 2 million yrs, which corresponds to the results of Figure 4-10. It is interesting to note that for almost the entire simulation three out of five points near the repository outline have saturations greater than the 65 percent potential corrosion-initiation level.

Figure 4-12 depicts the saturation contours corresponding to the pressure head results of Figure 4-10. The areas where the SC and GD faults force the geologic units to undulate, west and east of Yucca Crest, are clearly near fully saturated conditions (levels greater than 99.5 percent), an indication that these areas may be potential perched water zones. It is also worth noticing the very dry conditions the PTn unit is under, exhibiting saturations within the 2 to 20 percent range when units around it are at saturations greater than 80 percent. It should be mentioned, however, that the continuity of the extremely dry PTn condition breaks down right above the areas where perched water develops. These observations are consistent with the flow velocity results, presented in Figure 4-13. In this figure a contour plot of the $\log_{10}$ of the magnitude of the flow velocity is shown, superimposed by arrows indicating the direction of flow. A zone of high flow velocities is associated with the PTn unit to the east of Yucca Crest, exhibiting velocities three to four orders of magnitude higher than its surroundings. Moreover, this flow is for the most part lateral along the stratification imposed by the PTn unit with the exception of the areas near the SC and GD faults, which clearly demonstrate a "funneling" effect downwards. Similar observations can be made at the PPw-BFw interface.

As can be seen in Figure 4-13, a substantial variability of flow velocity magnitudes and directions exists. Thus, as mentioned before, statistics of these results are derived and presented in Figures 4-14 through 4-18. Figure 4-14 presents a histogram of the flow velocity direction for every computational cell in the flow domain. Values in velocity direction between –90 and –45 degrees correspond to predominantly downward sub-vertical flow. Sub-horizontal flow is indicated by values between –45 and +45 degrees. Finally, values between +45 and +90 degrees correspond to upward sub-vertical flow. In this case, with uniform infiltration over cross section A-A', it can be readily seen that the histogram is almost exponentially decaying from left (–90) to right (+90), a clear indication that the majority of flow is vertical and downwards. The CDF associated with this histogram is more revealing and is presented in Figure 4-15. One can now easily make quantitative inferences as to which is the dominant direction of flow. For example, in this figure it can be observed that 75 percent of the cells have a direction of flow between –90 and –45 degrees.

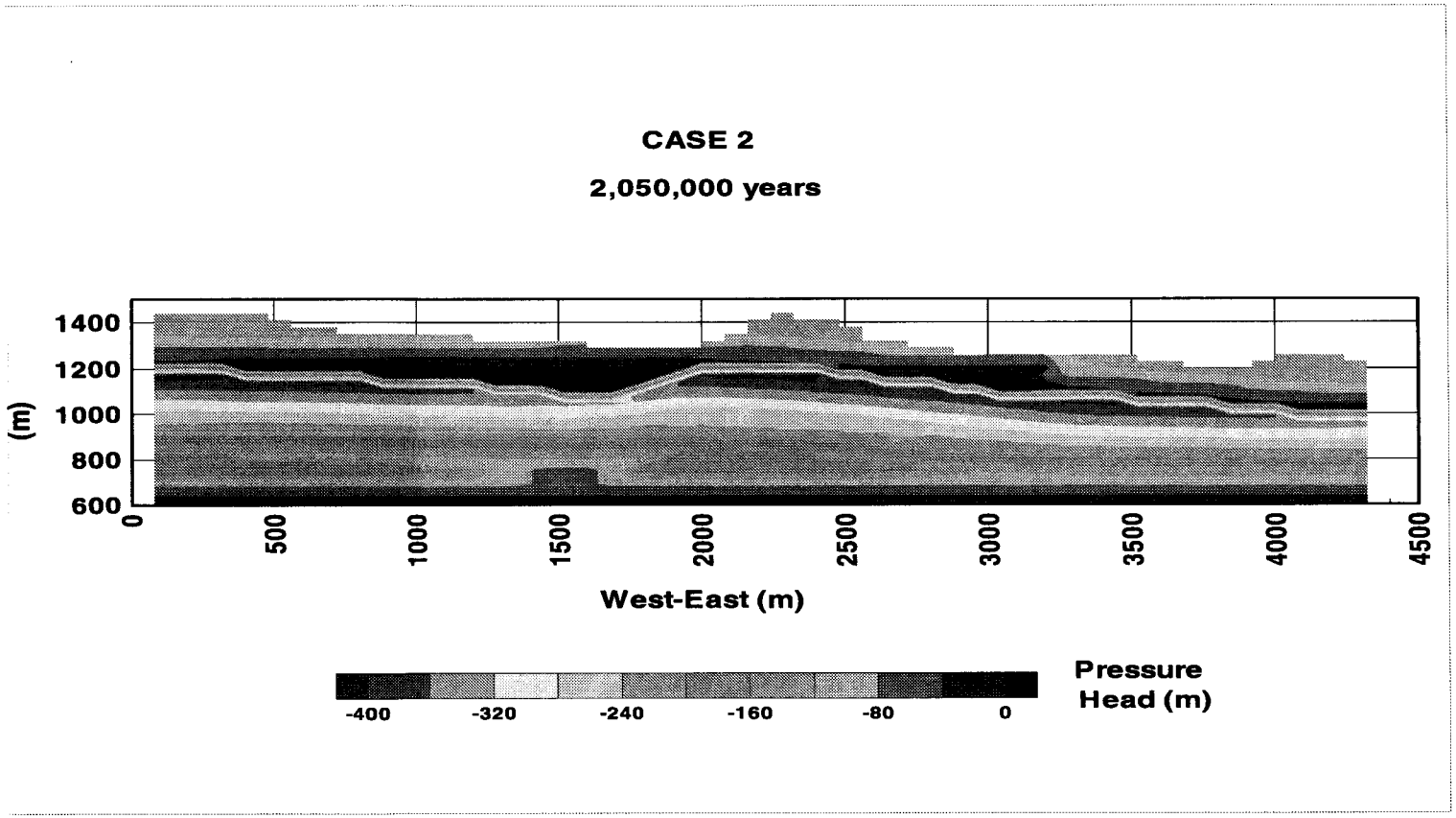

Figure 4-10. Pressure head contours for cross section A-A' under uniform infiltration

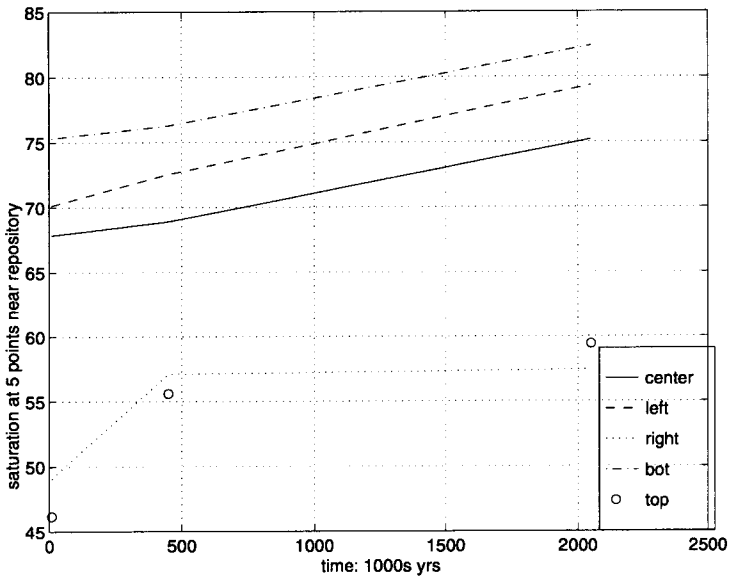

Figure 4-11. Saturation time history at five points near the repository outline for cross section A-A' under uniform infiltration

Figures 4-16 and 4-17 present the phase diagram-type of plot that correlates statistics of flow direction and magnitude. The interest for such discriminate classification is clear; not only one must know whether the majority of flow is vertical and downwards, but also it is of great interest to know whether this flow pattern is associated with the higher velocity magnitudes. The following clarifications are offered to facilitate understanding this type of plot. If all cells had velocity directions and magnitudes such that all statistics fell on a horizontal line passing near –90, vertical downwards flow with a variety of magnitudes could be inferred. A uniform cloud of symbols in this plot would be an indication of the fact that no specific pattern can be extracted from these flow velocities and magnitudes. Finally, a tightly convergent cloud near the right and bottom corner of this plot is an indication that not only the majority of flow is vertical and downwards but also that this direction of flow is characterized by high velocities. Indeed, this is the case in Figure 4-16. It appears that the majority of cells in this cross section have a direction of flow between –90 and –45 (75 percent as shown earlier) and $\log_{10}$ velocity magnitudes between –12 and –10.5. It is worth noticing that there exist faster pathways since $\log_{10}$ velocity magnitudes between –10.5 and –9.5 are shown in this plot. These velocities, however, are associated with sub-horizontal flows (presumably fast lateral flows along the PTn unit). Figure 4-17 depicts a plot similar to the one shown in Figure 4-16. The only difference here is that the analysis is performed for the subset of computational cells below the repository outline horizon. A comparison between Figures 4-16 and 4-17 reveals that the underlying statistics are similar for the whole domain and its subset below the repository. Perhaps the only difference is that there do not appear to exist so many perfectly vertical and downward flow components. Even though, again, the majority of flow is vertical and fast, the pattern is more uniformly distributed between the [-90, -45] and [–12, –11] coordinates.

Finally, Figure 4-18 shows the CDF of the $\log_{10}$ velocity magnitude for the cells below the repository outline. As indicated in Figures 4-6 and 4-7, a CDF that appears to be a straight line with a positive slope is an indication of a loguniform flux distribution. Similarly, a CDF that is of sigmoid

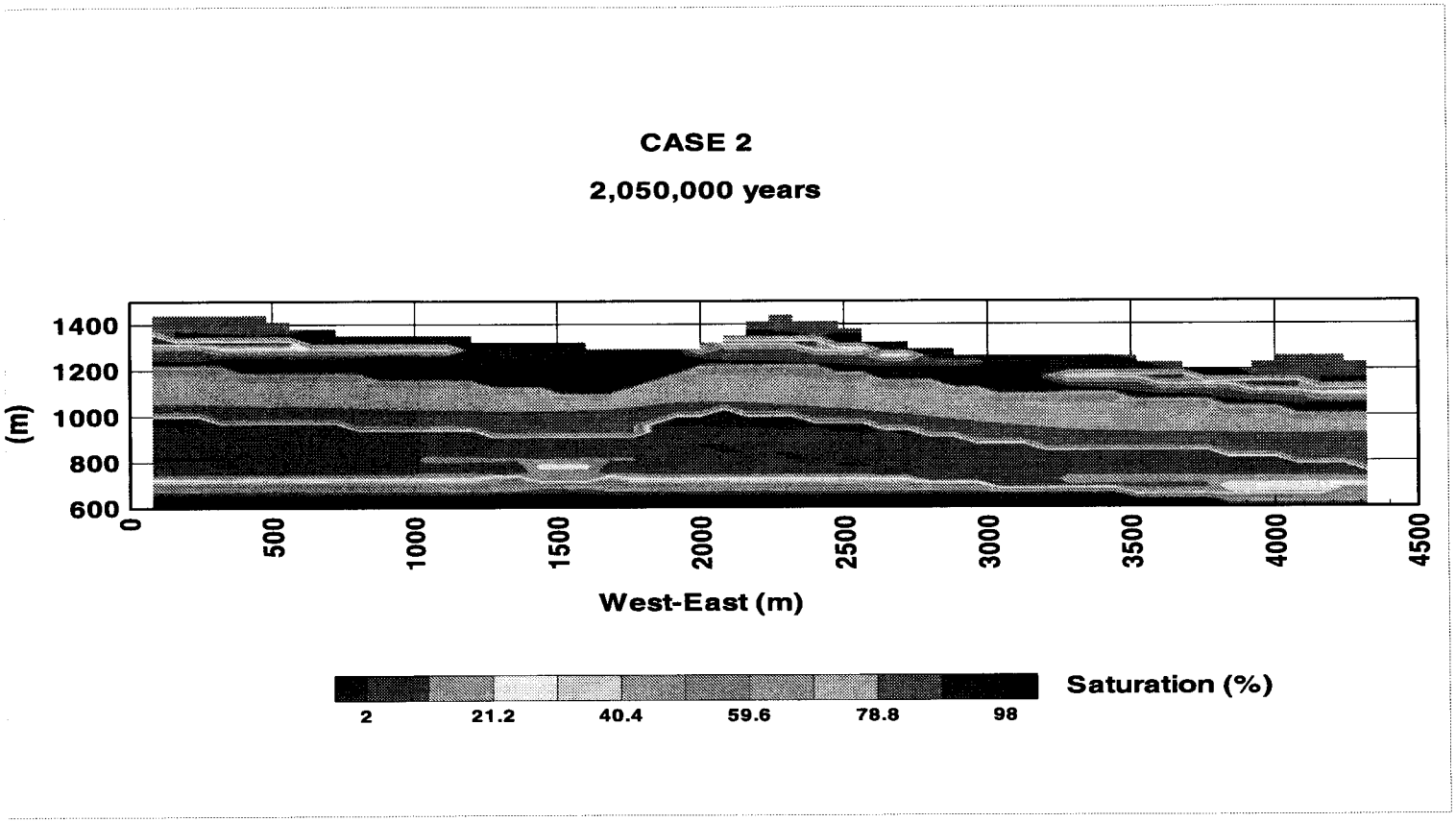

Figure 4-12. Saturation contours for cross section A-A' under uniform infiltration

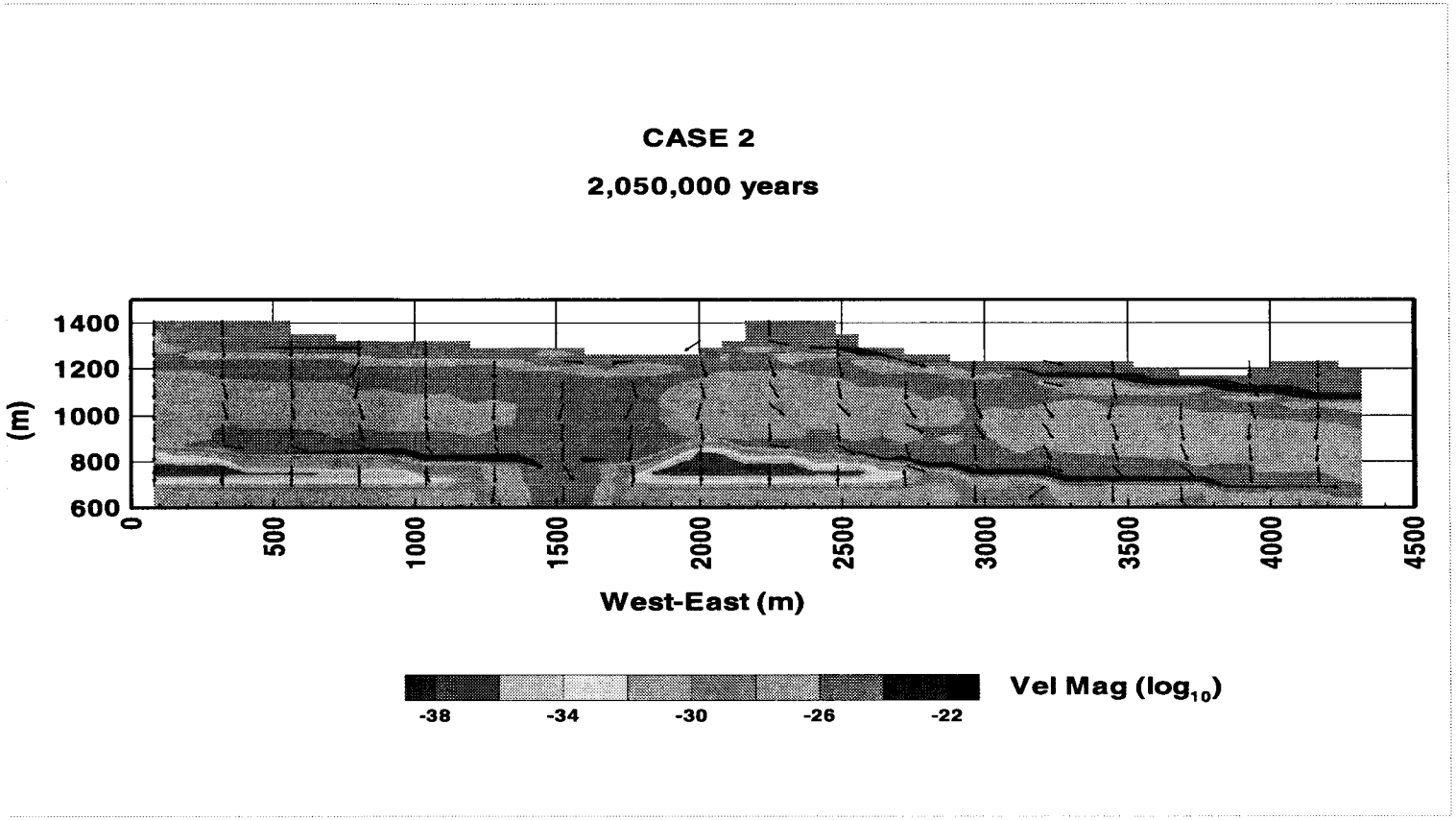

Figure 4-13. Flow velocity magnitude contours and direction of flow for cross section A-A' under uniform infiltration

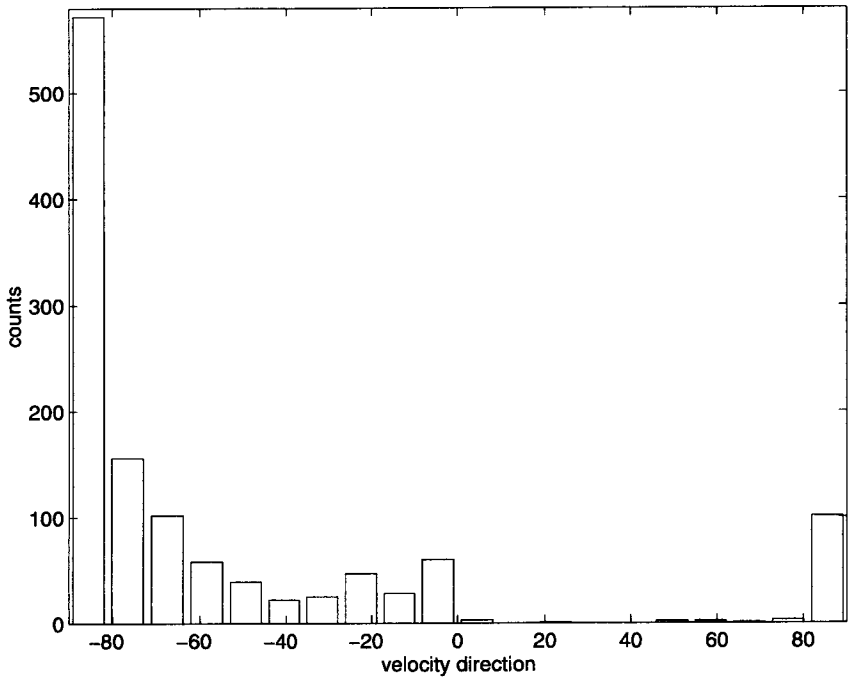

Figure 4-14. Histogram of flow velocity direction for cross section A-A' under uniform infiltration

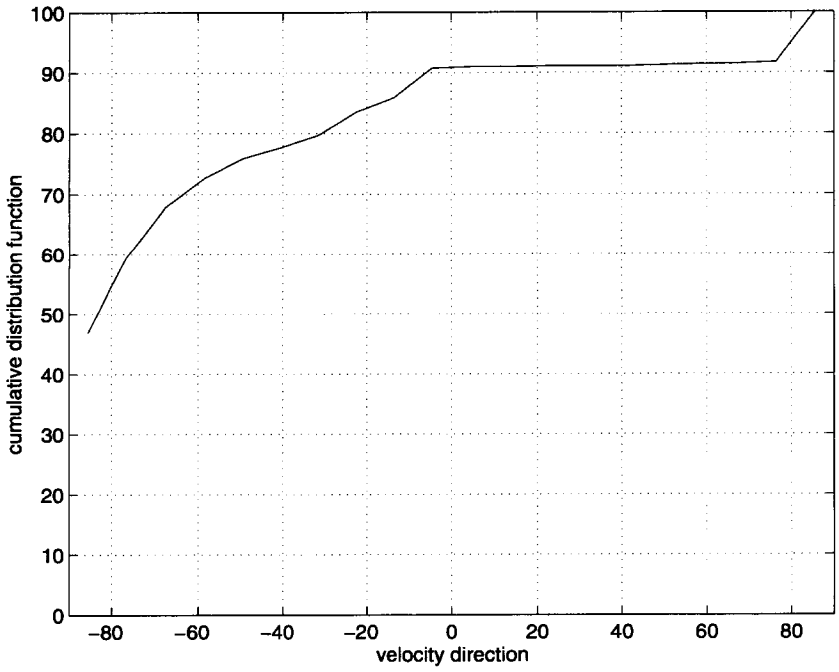

Figure 4-15. CDF of histogram of flow velocity direction for cross section A-A' under uniform infiltration

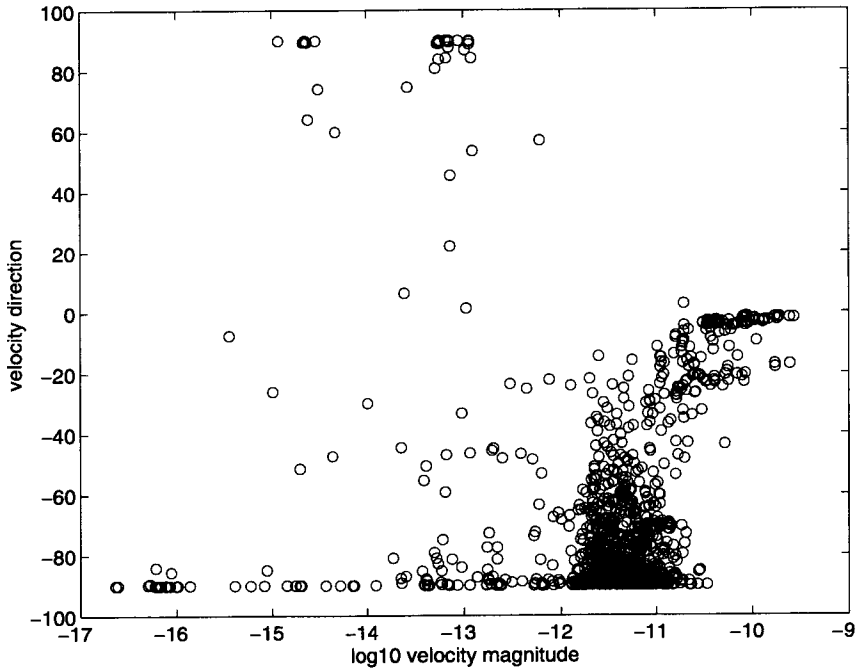

Figure 4-16. Correlation diagram between velocity magnitude and direction for cross section A-A' under uniform infiltration (every cell)

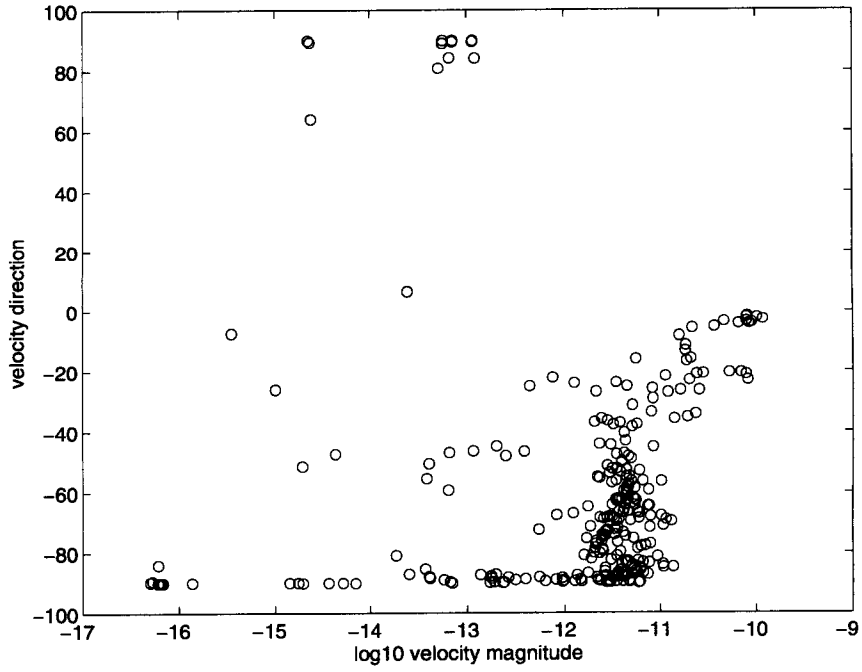

Figure 4-17. Correlation diagram between velocity magnitude and direction for cross section A-A' under uniform infiltration (only cells below the repository)

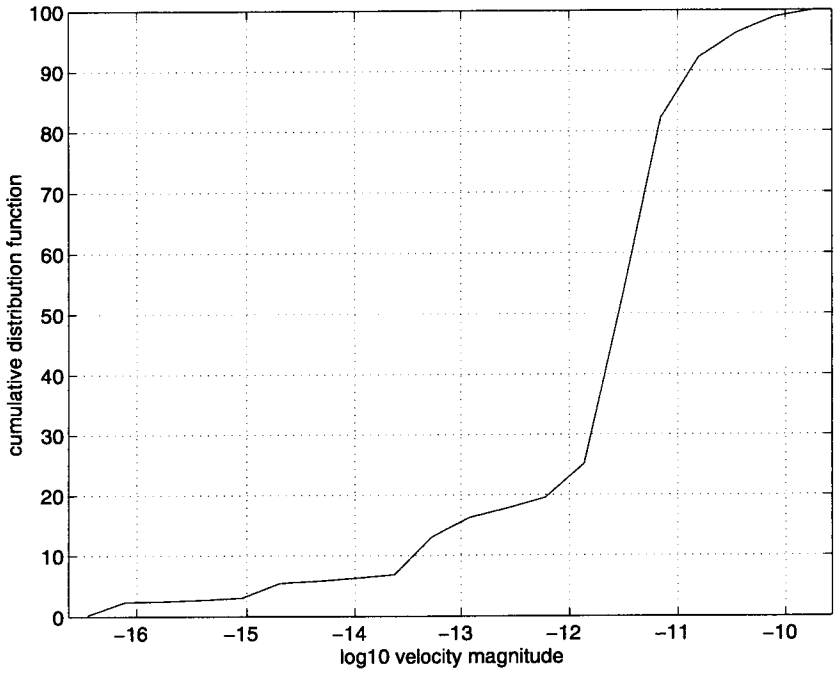

Figure 4-18. CDF of histogram of flow velocity magnitude for cross section A-A' under uniform infiltration

nature and appears to be reaching an asymptotic value at some point is an indication of an exponential flux distribution. The results of this simulation are quite interesting in the sense that, as depicted in Figure 4-18, a combination of the two behaviors is observed. One, based on the CDF up to a value of −12, can perhaps postulate the existence of a loguniform distribution of fluxes crossing the repository outline. However, one can also equally easily postulate an exponential distribution based on the CDF for values ranging between −16 and −9.5. The existence of a mixed-type distribution, whereby the flux is loguniformly distributed up to a certain magnitude and exponentially distributed for the whole range is perhaps a plausible hypothesis.

Figures 4-19 and 4-20 correspond to results of a flow simulation at steady state conditions under a focused infiltration rate of 1 mm/yr, applied over six computational cells immediately to the west of Yucca Crest at the bottom of the Solitario Canyon. This boundary condition corresponds to a SFI of approximately 4.5. Again, as indicated in Figure 4-19, the saturation levels at the repository horizon are high, ranging from 70 to 80 percent at the asymptotic value for three out of five sampling points. The importance of the location of the repository, relative to the area where infiltration is applied, is evident.

The bottom, left and center points have higher saturations than the right and top points, which are farther away from the area where the focused infiltration is being applied. Figure 4-20, compared to Figure 4-16, indicates that focusing infiltration had minimal effects on the statistics of the moisture fluxes in the deep parts of the mountain. However, a decrease in the sub-horizontal fast pathways is apparent since no velocity magnitude is greater than −10.

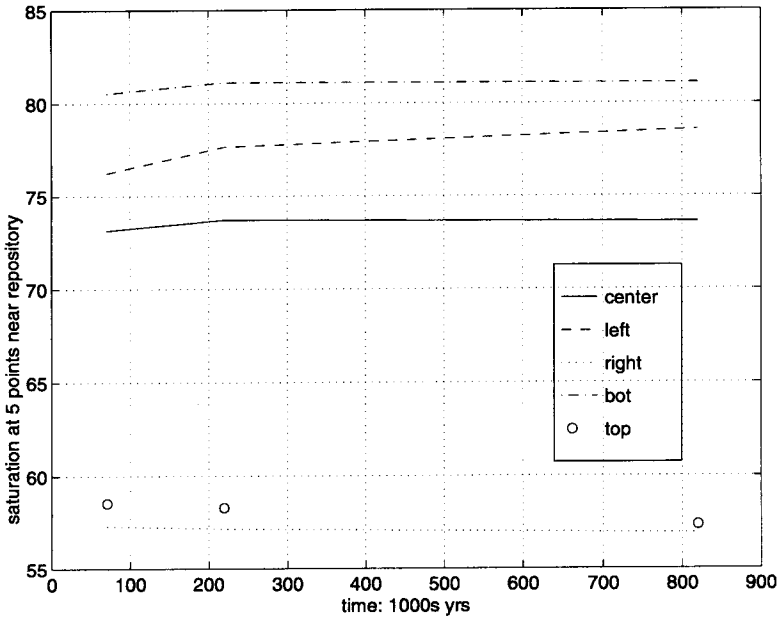

Figure 4-19. Saturation time history at five points near the repository outline for cross section A-A' under focused infiltration

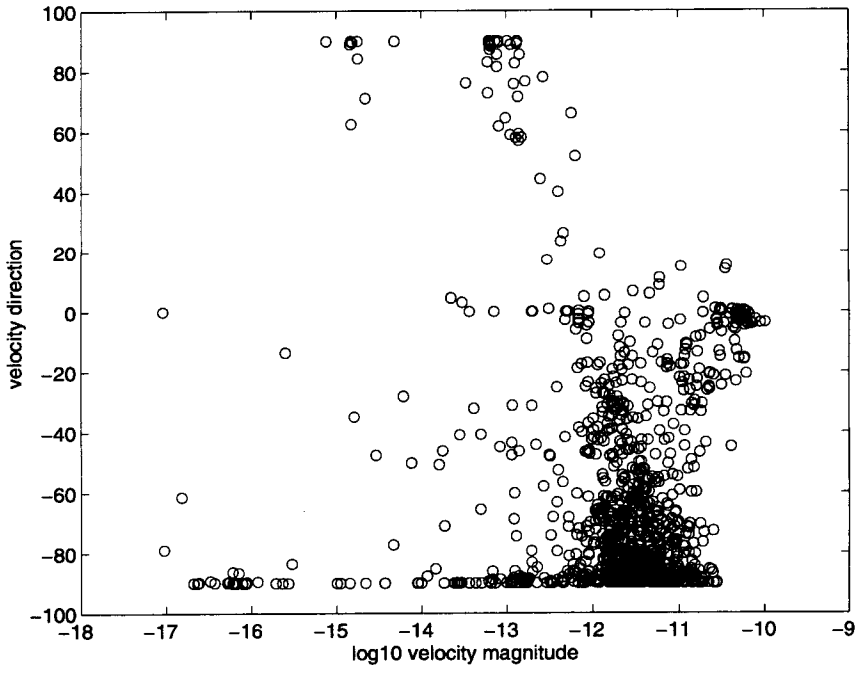

Figure 4-20. Correlation diagram between velocity magnitude and direction for cross section A-A' under focused infiltration (every cell)

4.2.2 Faulted Cross Section (B-B')

The fundamental difference between the flow results of cross sections B-B' and A-A' can be seen in Figure 4-21, which depicts saturation contours for the draining simulation. The profound effect of an important structural feature, such as the SC fault, on the saturation pattern is clear. Most of the units that are down dip of the SC fault have very low saturations, ranging from less than 2 percent to 10 percent. The barrier-like behavior of the PTn unit is also perceptible.

A uniform infiltration rate of 0.15 mm/yr was applied over the whole cross section. Figure 4-22 presents the correlation of velocity magnitude and direction diagram for this simulation. Once again, a very strong vertical and fast component of flow exists. However, a uniform distribution of sub-vertical and sub-horizontal velocities also exists. Figure 4-23 depicts the CDF of the $\log_{10}$ velocity magnitude, which may be indicating the existence of a three-type mixed flux distribution; one mode following a loguniform and two modes following an exponential distribution.

A focused infiltration simulation with a net infiltration rate of 1.72 mm/yr was also conducted. This simulation applied the infiltration over 5 cells at the PTn outcrop at the west of the SC fault; thus, a SFI value of 5.1 was imposed. Figure 4-24 shows a contour plot of the flow velocity magnitude and directions. Sub-vertical flow components are evident in the host rock (TSw1 and TSw23) and CHn units at the east side of the SC fault. Predominantly vertical flow exists at the west side of the SC fault. It is also worth noticing the very strong (two to three orders of magnitude higher) flow velocities existing within the CHn units as a manifestation of a hydraulic connection being established between the area where focused infiltration is applied and the GD fault area, where a funneling effect is apparent.

For the same simulation, one can observe the saturation levels at the repository horizon in Figure 4-25. All sampling points have high saturation levels, greater than 75 percent at all times with the center, right, and top points exhibiting decreasing saturations. Figure 4-26 shows the velocity magnitude-direction correlation plot. Comparing Figures 4-26 and 4-22, one can see that focusing infiltration causes a deviation from the predominant vertical, downwards and fast pattern. A more uniform distribution of fast pathways corresponding to a variety of sub-vertical and sub-horizontal directions of flow is present, perhaps due to the strong lateral interfacial flow components. Figure 4-27 depicts the CDF of the velocity magnitude, indicating the familiar mixed-type loguniform-exponential flux distribution.

Finally, another focused infiltration simulation with the same net infiltration rate of 1.72 mm/yr was conducted for cross section B-B'. This time, however, the infiltration was applied over 9 cells at the TSw23 outcrop at the west of the SC fault, imposing a SFI of 2.9. This simulation is, partly, in response to the State of Nevada's concerns regarding focused recharge along the SC fault, which would feed water directly into the host rock horizon. Figure 4-28, when compared to Figure 4-25, indicates that this focusing mechanism does not appear to substantially increase the saturation levels at the repository horizon. The saturation for the bottom point increased from 88 to 88.5 percent and the left point increased from 89 to 90 percent. All other points of the repository maintained the same levels of saturation. Similarly, Figure 4-29 indicates that the same flow direction and magnitude correlation patterns exist for the two focusing mechanisms. Comparing Figures 4-29 and 4-26 one can observe only minor differences in the correlation patterns.

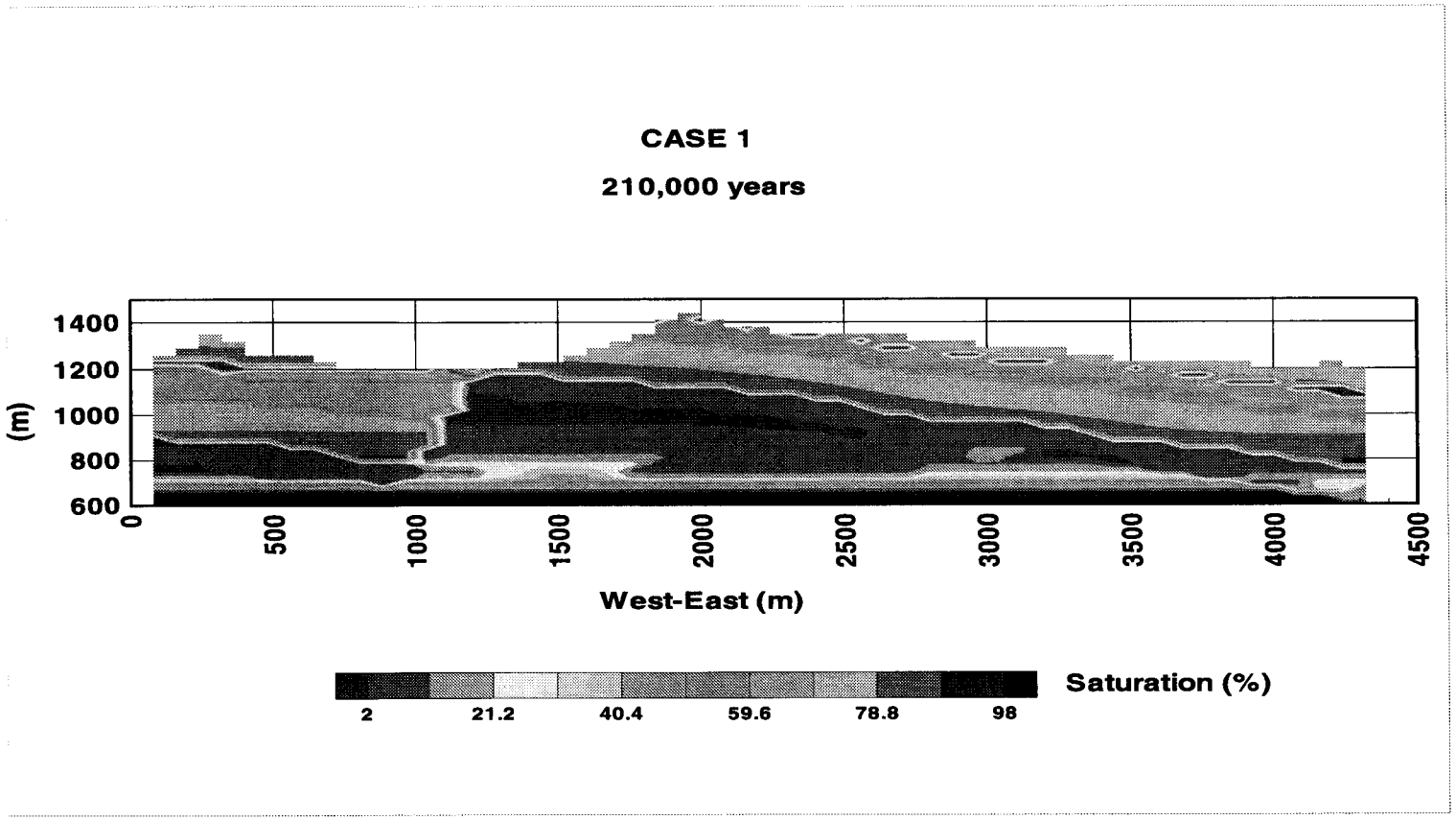

Figure 4-21. Saturation contours for cross section B-B' under draining conditions

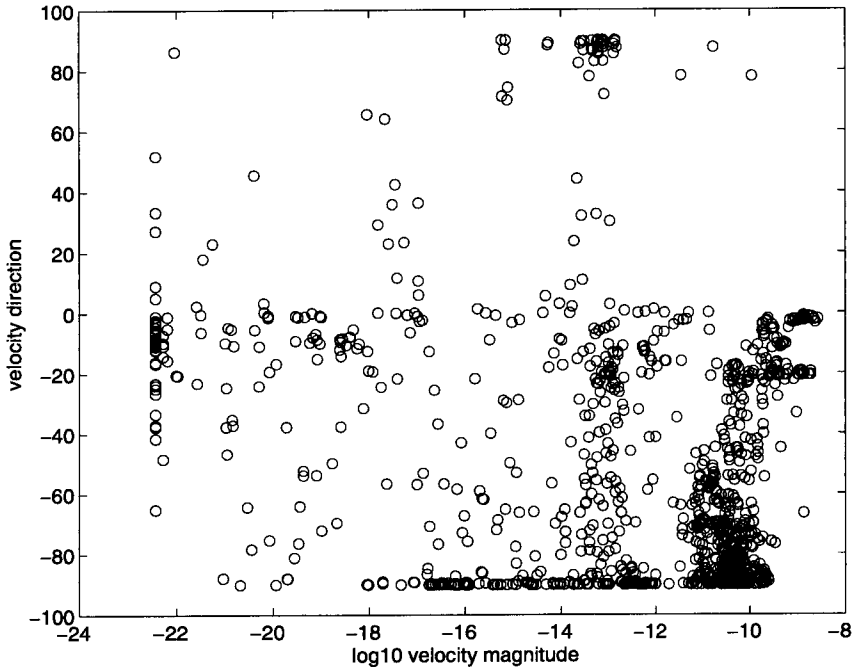

Figure 4-22. Correlation diagram between velocity magnitude and direction for cross section B-B' under uniform infiltration (every cell)

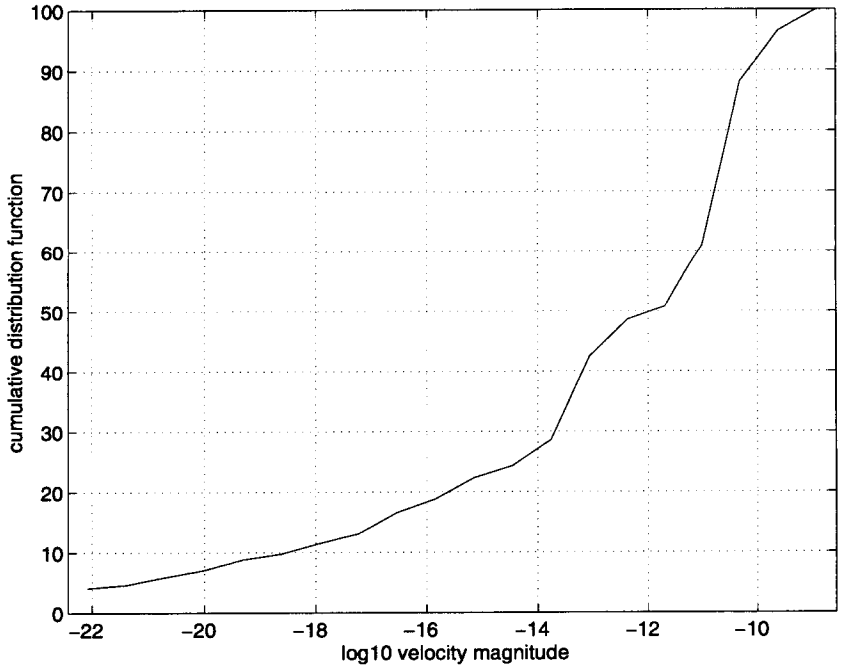

Figure 4-23. CDF of histogram of flow velocity magnitude for cross section B-B' under uniform infiltration

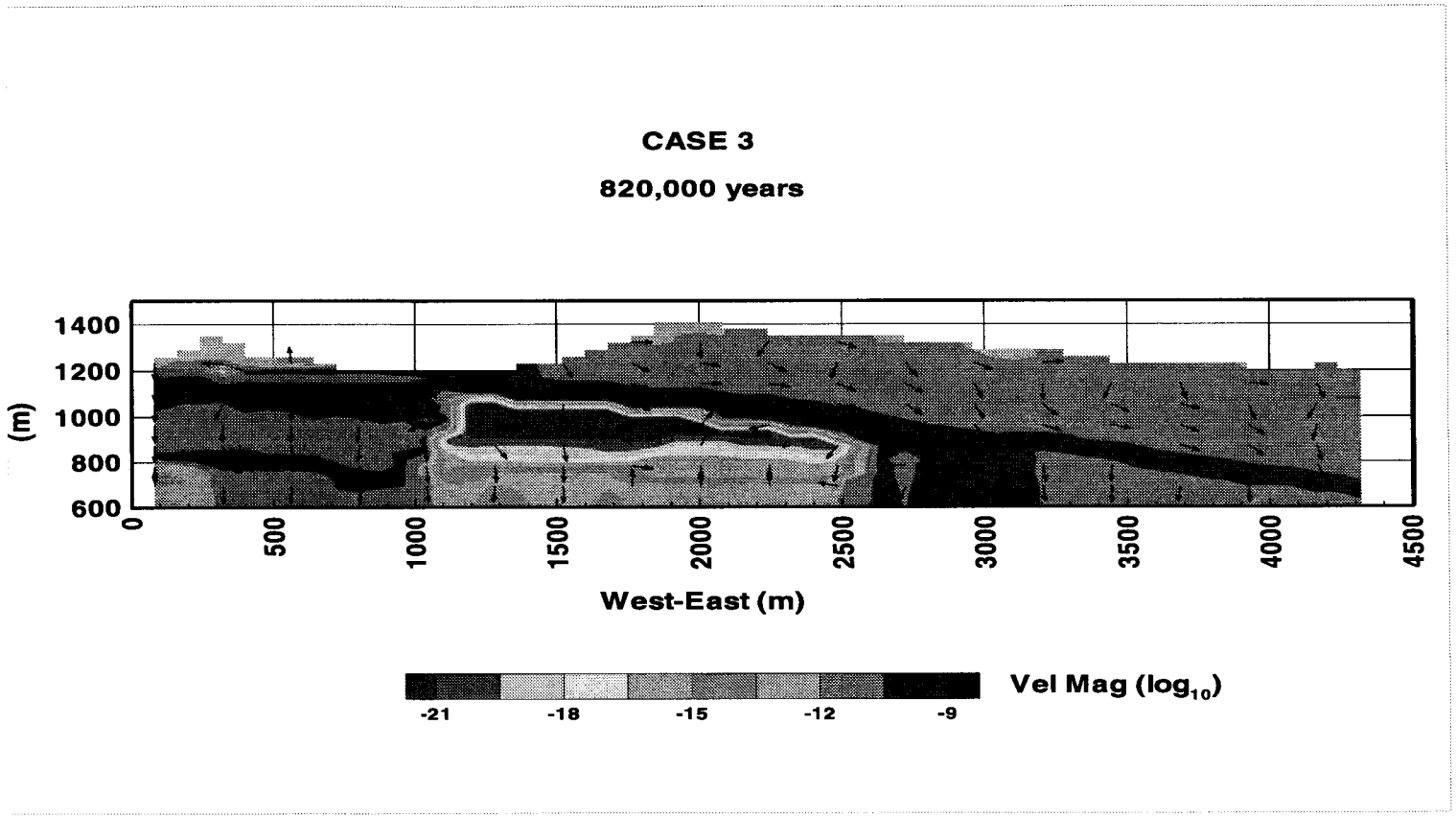

Figure 4-24. Flow velocity magnitude contours and direction of flow for cross section B-B' under focused infiltration at the PTn outcrop

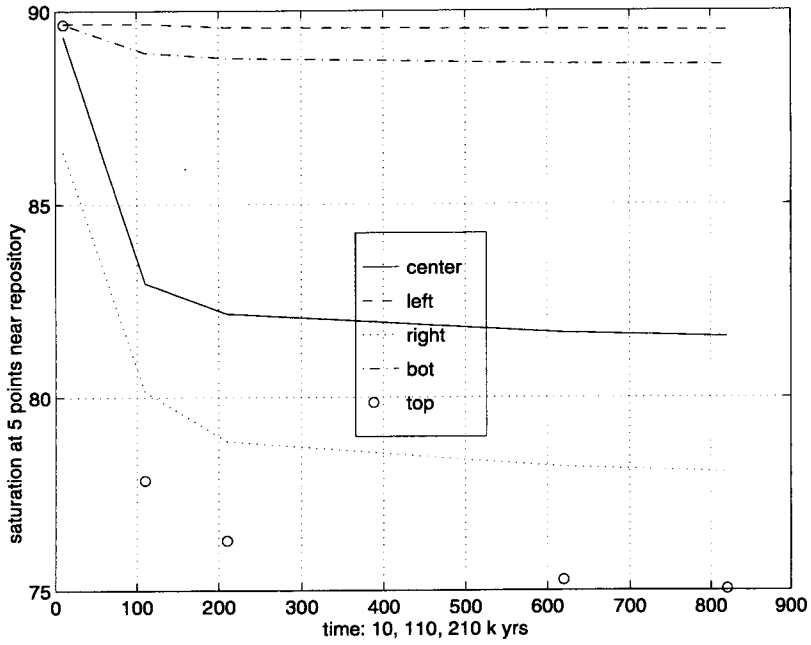

Figure 4-25. Saturation time history at five points near the repository outline for cross section B-B' under focused infiltration at the PTn outcrop

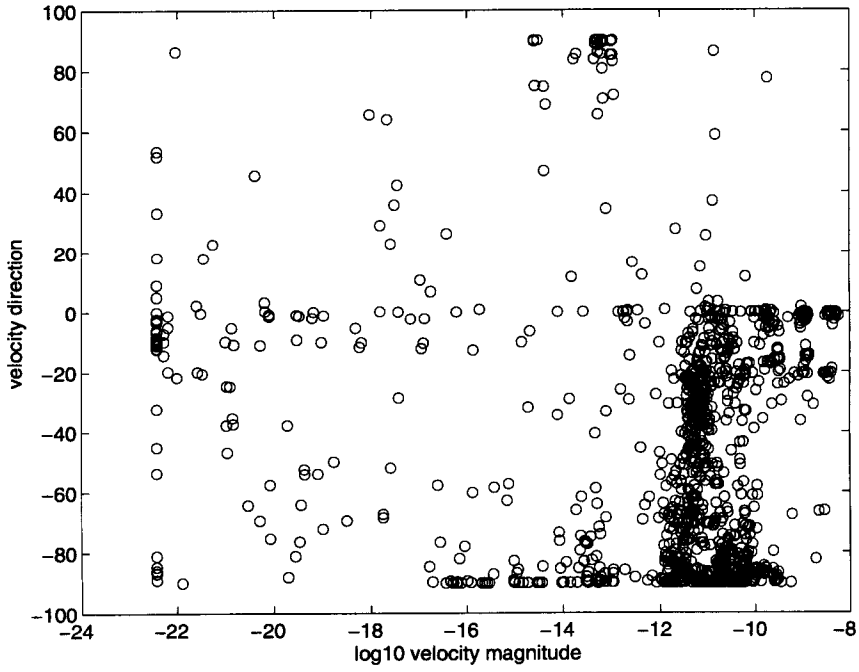

Figure 4-26. Correlation diagram between velocity magnitude and direction for cross section B-B' under focused infiltration at the PTn outcrop (every cell)

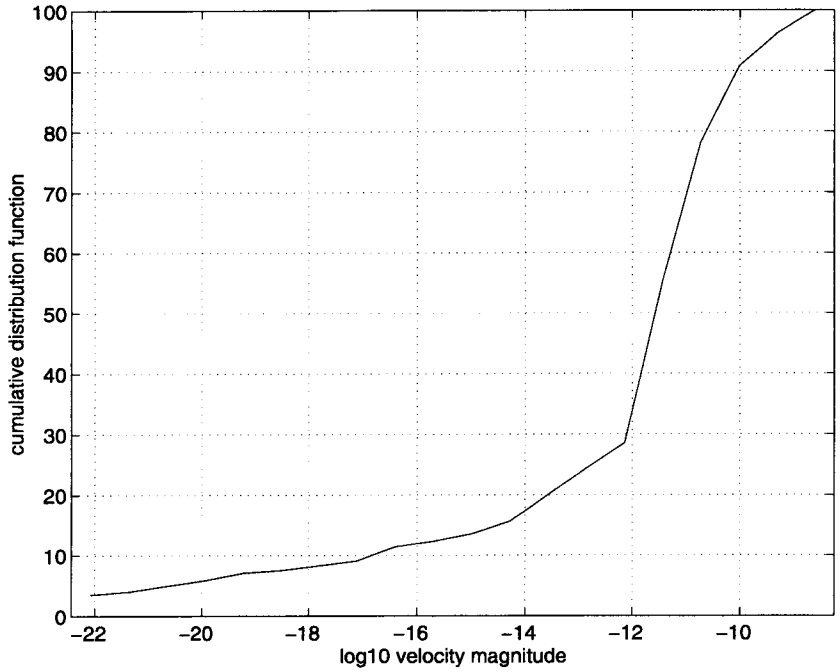

Figure 4-27. CDF of histogram of flow velocity magnitude for cross section B-B' under focused infiltration at the PTn outcrop

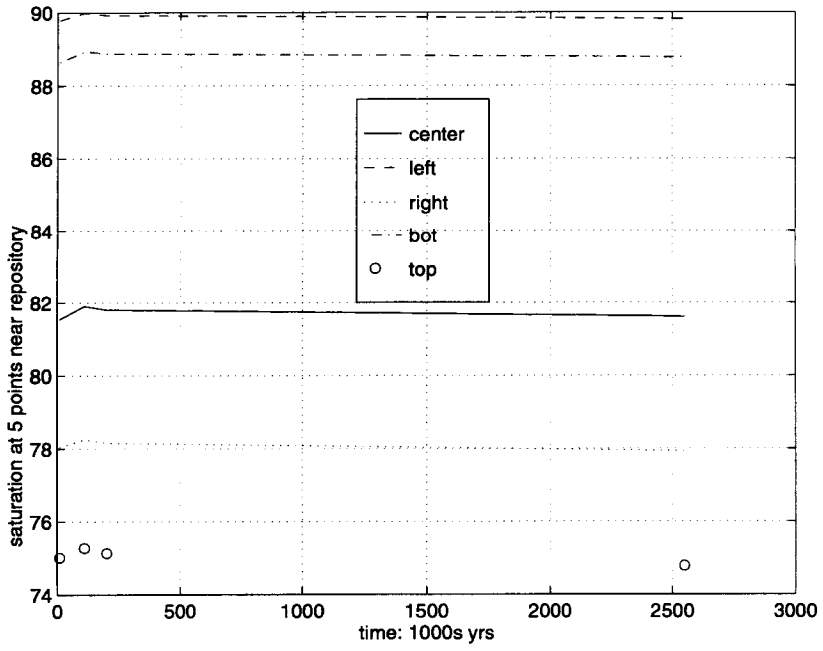

Figure 4-28. Saturation time history at five points near the repository outline for cross section B-B' under focused infiltration at the TSw23 outcrop

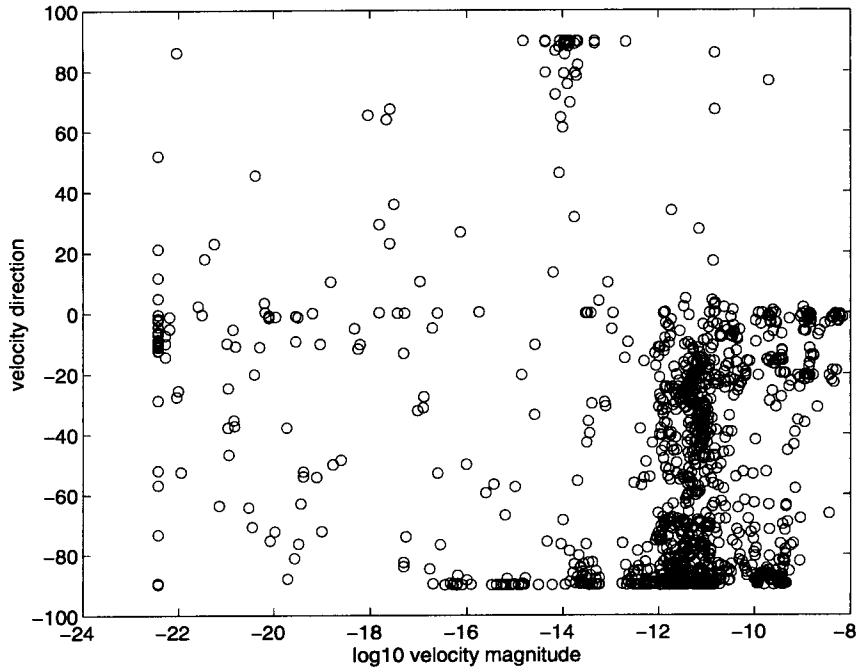

Figure 4-29. Correlation diagram between velocity magnitude and direction for cross section B-B' under focused infiltration at the TSw23 outcrop (every cell)

4.3 CONCLUSIONS OF THE DEEP PERCOLATION STUDY

Findings of this study are:

(i) The Paintbrush Tuff-nonwelded unit routinely exhibits lateral (along the dip of the unit) flow diversion, with the exception of the areas where it is broken by normal faults.

(ii) Juxtaposed geologic strata provide the opportunity for perching of water to occur.

(iii) The dominant flow pattern at the two YM site cross sections, studied here, is vertical.

(iv) Focusing recharge (preferentially) along the SC fault has an important effect on the flow velocity patterns by increasing the lateral component.

(v) A mixed (loguniform and exponential) distribution of water fluxes crossing the repository horizon appears to be plausible.

(vi) A PDF for the percolation flux crossing the repository horizon at the two cross sections studied has been developed. This PDF can be used in future IPA Phase 3 analyses.

5 CONCLUSIONS

This numerical modeling study was motivated by the need to provide physically based estimates of infiltration and deep percolation rates for the YM site, to understand the impact of spatial or temporal averaging, to determine the meteorologic parameters that most significantly influence the calculation of net infiltration, and to evaluate the hydrologic role of selected structural features (e.g., the Paintbrush Tuff nonwelded unit and the Solitario Canyon fault).

The shallow infiltration study employed numerical simulations of coupled moisture and energy transport in homogeneous porous media and evaluated responses of the near-surface soil profile. A ten-yr sequence of weather data was used and provided some counter-intuitive results, which indicate that media with higher values of permeability allow less liquid water to percolate into the deeper parts of the rock. The major conclusions of this study are: (i) the first portion of a response function for net long-term infiltration into the skin of YM is developed. The simplest case, response of infiltration to various hydraulic properties of deep minimally vegetated alluvium is presented; (ii) a deep alluvium with permeability less than 10^{-6} cm^2 would be expected to dry out, even in the absence of vegetation, thus having negligible infiltration under YM conditions; (iii) for deep alluvia with permeabilities greater than the dryout permeability, a range of permeability spanning 5 orders of magnitude is found to have a concommitant range in net deep infiltration of nearly 3 orders of magnitude; (iv) surprisingly, net deep infiltration varies inversely with permeability for the higher-permeability media, so that permeability may be a misleading indicator of infiltration into a porous continuum; (v) lower-permeability media develop an evaporation-limiting dryout zone sooner than higher-permeability media, thereby allowing less evaporation and leaving more water for net infiltration; and (vi) the highest net long-term infiltration rates occur for media that saturate for only the largest rainfall events. When a medium saturates for small events, much of the rainfall is diverted into runoff and prevented from entering the soil column. When a medium easily accepts all rainfall, it also easily returns the moisture to the surface to be reclaimed as evaporation, leaving less for infiltration.

A deep percolation study was also presented that addressed the effect of spatial and temporal averaging of infiltration on the speed with which a moisture front propagates within a block of homogeneous rock. This study demonstrated that increasing spatial focusing of infiltration does not necessarily translate to increased moisture plume speeds or penetration depths since extensive lateral flows are initiated under such conditions. Specifically, the major conclusions of this study are: (i) the area under the focused percolation is substantially wetter for the higher focusing index. Furthermore, it is associated with extensive lateral flow; (ii) the moisture penetration depth is consistently underestimated in cases when a temporally averaged infiltration signal is employed; and (iii) as infiltration deviates from a temporally averaged signal and approaches a sinusoidal the effects of spatial focusing on moisture penetration depth become insignificant.

Finally, a numerical study of deep percolation at the YM site was conducted. Two vertical, west-east cross sections were extracted from the current version of the CNWRA hydro-geostratigraphic model of YM and results from 2D flow simulations, testing several focused recharge cases, were analyzed. This study provided an improved probability density function for percolation through the repository horizon at the two cross sections studied and demonstrated that focusing recharge along the Solitario Canyon fault area increases the lateral flow component but does not affect substantially the magnitude or statistical nature of the flux at the repository level. More specifically, this study concluded that: (i) the PTn unit routinely exhibits lateral flow diversion, with the exception of the areas where it is broken by normal faults;

(ii) juxtaposed geologic strata provide the opportunity for substantial perching of water to occur; (iii) the dominant flow pattern is vertical at the two YM site cross sections studied here; (iv) focusing recharge along the SC fault has an important effect on the flow velocity patterns by increasing the lateral component, but does not significantly affect flow conditions at the repository horizon; (v) a mixed (loguniform and exponential) distribution of water fluxes crossing the repository horizon appears to be plausible; and (vi) an improved PDF for the percolation flux crossing the repository horizon has been developed for use in future IPA Phase 3 analyses.

6 REFERENCES

Ababou, R., and A.C. Bagtzoglou. 1993. *BIGFLOW: A Numerical Code for Simulating Flow in Variably Saturated, Heterogeneous Geologic Media, Theory and User's Manual, Version 1.1.* NUREG/CR-6028, CNWRA 92-026. Washington, DC: Nuclear Regulatory Commission.

Czarnecki, J.B. 1990. *Geohydrology and Evapotranspiration at Franklin Lake Play, Inyo County, California.* Open-File Report 90-356. Denver, CO: U.S. Geological Survey.

de Vries, D.A. 1958. Simultaneous tranfer of heat and moisture in porous media. *EOS Transactions of the American Geophysical Union* 39(5): 909–916.

DeWispelare, A.R., L.T. Herren, M.P. Miklas, and R.T. Clemen. 1993. *Expert Elicitation of Future Climate in the Yucca Mountain Vicinity.* CNWRA 93-016. San Antonio, TX: Center for Nuclear Waste Regulatory Analyses.

Electric Power Research Institute. 1990. *Demonstration of a Risk-Based Approach to High-Level Waste Repository Evaluation.* EPRI NP-7056. Palo Alto, CA: Electric Power Research Institute.

Electric Power Research Institute. 1992. *Demonstration of a Risk-Based Approach to High-Level Waste Repository Evaluation Phase 2.* EPRI TR-100384. Palo Alto, CA: Electric Power Research Institute.

Fayer, M.J., and T.L. Jones. 1990. *UNSAT-H Version 2.0: Unsaturated Soil Water and Heat Flow Manual.* PNL-6779. Richland, WA: Pacific Northwest Laboratory.

Flint, A.L., and L.E. Flint. 1994. Spatial distribution of potential near surface moisture flux at Yucca Mountain. *Proceedings of Fifth International High Level Radioactive Waste Management Conference.* LaGrange Park, IL: American Nuclear Society: 2,352–2,358.

Freeze, R.A., and J.A. Cherry. 1979. *Groundwater.* Englewood Cliffs, NJ: Prentice-Hall.

Gee, G.W. 1966. *Water Movement in Soils as Influenced by Temperature Gradients.* Ph.D. Thesis. Pullman, WA: Washington State University.

Guertal, W., A.L. Flint, L.L. Hofmann, and D.B. Hudson. 1994. Characterization of a desert soil sequence at Yucca Mountain, NV. *Proceedings of the Fifth Annual High-Level Radioactive Waste Management Conference.* LaGrange Park, IL: American Nuclear Society: 2,755–2,763.

Gureghian, A.B., A.R. DeWispelare, and B. Sagar. 1994. Sensitivity and probabilistic analyses of the impact of climatic conditions on the infiltration rate in a variably saturated multilayered geologic medium. *Proceedings of the Fifth Annual High-Level Radioactive Waste Management Conference.* LaGrange Park, IL: American Nuclear Society: 1,622–1,633.

Hevesi, J.A., J.D. Istok, and A.L. Flint. 1992a. Precipitation estimation in mountainous terrain using multivariate geostatistics: Part I: Structural analysis. *Journal of Applied Meteorology* 31(7): 661–676.

Hevesi, J.A., A.L. Flint, and J.D. Istok. 1992b. Precipitation estimation in mountainous terrain using multivariate geostatistics: Part II: Isohyetal Maps. *Journal of Applied Meteorology* 31(7): 677–688.

Hevesi, J.A., and A.L. Flint. 1993. The influence of seasonal climatic variability on shallow infiltration at Yucca Mountain. *Proceedings of the Fourth Annual High-Level Radioactive Waste Management Conference*. LaGrange Park, IL: American Nuclear Society: 122–131.

Hevesi, J.A., A.L. Flint, and L.E. Flint. 1994a. Verification of a 1-dimensional model for predicting shallow infiltration at Yucca Mountain. *Proceedings of the Fifth Annual High-Level Radioactive Waste Management Conference*. LaGrange Park, IL: American Nuclear Society: 2,323–2,332.

Hevesi, J.A., D.S. Ambos, and A.L. Flint. 1994b. A preliminary characterization of the spatial variability of precipitation at Yucca Mountain, Nevada. *Proceedings of Fifth International High Level Radioactive Waste Management Conference*. LaGrange Park, IL: American Nuclear Society: 2,520–2,529.

Hudson, D.B., A.L. Flint, and W.R. Guertal. 1994. Modeling a ponded infiltration experiment at Yucca Mountain, NV. *Proceedings of the Fifth Annual High-Level Radioactive Waste Management Conference*. LaGrange Park, IL: American Nuclear Society: 2,168–2,174.

Jury, W.A. 1973. *Simultaneous Transport of Heat and Moisture Through a Medium Sand*. Ph.D. Thesis. Madison, WI: University of Wisconsin.

Manteufel, R.D., and R.G. Baca. 1995. *Iterative Performance Assessment Phase 3: Status of Activities*. CNWRA 95-007. San Antonio, TX: Center for Nuclear Waste Regulatory Analyses.

Milly, P.C.D., and P.S. Eagleson. 1980. *The Coupled Transport of Water and Heat in a Vertical Soil Column Under Atmospheric Excitation*. Ralph Parsons Laboratory Report No. 258. Cambridge, MA: Massachusetts Institute of Technology.

Nuclear Regulatory Commission. 1992. *Initial Demonstration of the NRC's Capability to Conduct a Performance Assessment for a High-Level Waste Repository*. NUREG-1327. Washington, DC: Nuclear Regulatory Commission.

Nuclear Regulatory Commission. 1995. *Phase 2 Demonstration of the NRC's Capability to Conduct a Performance Assessment for a High-Level Waste Repository*. NUREG-1464. Washington, DC: Nuclear Regulatory Commission. In press.

Ortiz, T.S., R.L. Williams, F.B. Nimick, B.C. Whittet, and D.L. South. 1985. *A Three-Dimensional Model of Reference Thermal/Mechanical and Hydrological Stratigraphy at Yucca Mountain, Southern Nevada*. SAND84-1076. Albuquerque, NM: Sandia National Laboratories.

Philip, J.R., and D.A. de Vries. 1957. Moisture movement in porous materials under temperature gradients. *EOS Transactions of the American Geophysical Union* 38(2): 222–232.

Richards, L.A. 1931. Capillary conduction of liquids through porous mediums. *Physics* 1: 318–333.

Sandia National Laboratories. 1992. *TSPA 1991: An Initial Total-System Performance Assessment for Yucca Mountain.* SAND91-2795. Albuquerque, NM: Sandia National Laboratories.

Sandia National Laboratories. 1994. *Total-System Performance Assessment for Yucca Mountain-SNL Section Iteration (TSPA-1993).* SAND93-2675. Albuquerque, NM: Sandia National Laboratories.

Sasamori, T. 1970. A numerical study of atmospheric and soil boundary layers. *Journal of Atmospheric Science* 27(8): 1,122–1,137.

Scott, R.B., and J. Bonk. 1984. *Preliminary Geologic Map (1:12,000 scale) of Yucca Mountain, Nye County, Nevada, with Geologic Cross Sections.* U.S. Geological Survey Open-File Report 84-494. Denver, CO: U.S. Geological Survey.

Sophocleous, M.A. 1978. *Analysis of Heat and Water Transport in Unsaturated-Saturated Porous Media.* Ph.D. Thesis. Edmonton, Canada: The University of Alberta.

Stirewalt, G.L., and D.B. Henderson. 1995a. A preliminary three-dimensional geological framework model for Yucca Mountain. *Proceedings of the Sixth Annual International High-level Radioactive Waste Management Conference.* LaGrange Park, IL: American Nuclear Society: 116–118.

Stirewalt, G.L., and D.B. Henderson. 1995b. *A Three-Dimensional Geological Framework Model for Yucca Mountain, Nevada, with Hydrologic Application: Report to Accompany 1995 Model Transfer to the Nuclear Regulatory Commission.* CNWRA 94-023 Rev. 1. San Antonio, TX: Center for Nuclear Waste Regulatory Analyses.

Stothoff, S.A. 1995. *BREATH Version 1.1—Coupled Flow and Energy Transport in Porous Media: Simulator Description and User Guide.* NUREG/CR-6333. Washington, DC: Nuclear Regulatory Commission.

U.S. Department of Energy. 1988. *Site Characterization Plan, Yucca Mountain Site, Nevada Research and Development Area, Nevada.* DOE/RW-0199. Washington, DC: U.S. Department of Energy.

U.S. Department of Energy. 1992. *Report of Early Site Suitability Evaluation of the Potential Repository Site at Yucca Mountain, Nevada.* Washington, DC: U.S. Department of Energy.

Wilson, M.L., J.H. Gauthier, R.W. Barnard, G.E. Barr, H.A. Dockery, E. Dunn, R.R. Eaton, D.C. Guerin, N. Lu, M.J. Martinez, R. Nilson, C.A. Rautman, T.H. Robey, B. Ross, E.E. Ryder, A.R. Schenker, S.A. Shannon, L.H. Skinner, W.G. Halsey, J.D. Gansemer, L.C. Lewis, A.D. Lamont, I.R. Triay, A. Meijer, and D.E. Morris. 1994. *Total-System Performance Assessment for Yucca Mountain—SNL Second Iteration (TSPA-1993).* SAND93-2675. Albuquerque, NM: Sandia National Laboratories.

Wittwer, C.S., G. Chen, and G.S. Bodvarsson. 1993. Studies of the role of fault zones on fluid flow using the site-scale numerical model of Yucca Mountain. *Proceedings of the Fourth International Conference on High-level Radioactive Waste Management.* LaGrange Park, IL: American Nuclear Society: 667–674.

Young, D.R., and P.S. Nobel. 1986. Predictions of soil-water potentials in the north-western Sonoran desert. *Journal of Ecology* 74: 143–154.